

# X-ray Structural and Functional Studies of the Three Tandemly Linked Domains of Non-structural Protein 3 (nsp3) from Murine Hepatitis Virus Reveal Conserved Functions\*

Received for publication, April 30, 2015, and in revised form, August 18, 2015. Published, JBC Papers in Press, August 19, 2015, DOI 10.1074/jbc.M115.662130

Yafang Chen<sup>‡</sup>, Sergey N. Savinov<sup>§1</sup>, Anna M. Mielech<sup>¶</sup>, Thu Cao<sup>‡</sup>, Susan C. Baker<sup>¶</sup>, and Andrew D. Mesecar<sup>‡#§||2</sup>

From the <sup>‡</sup>Department of Biological Sciences, the <sup>§</sup>Center for Cancer Research, and the <sup>¶</sup>Department of Biochemistry, Purdue University, West Lafayette, Indiana 47907 and the <sup>¶</sup>Department of Microbiology and Immunology, Stritch School of Medicine, Loyola University of Chicago, Maywood, Illinois 60153

**Background:** Coronavirus nsp3 is essential for virus replication.

**Results:** The structure of three tandemly linked domains of MHV nsp3 was determined.

**Conclusion:** A new domain was discovered within MHV nsp3, and the PLP2 domain of MHV nsp3 possesses both deubiquitinating and deISGylating activities.

**Significance:** Our studies provide a platform for further investigation of the role of coronaviral nsp3 in virus replication.

Murine hepatitis virus (MHV) has long served as a model system for the study of coronaviruses. Non-structural protein 3 (nsp3) is the largest nsp in the coronavirus genome, and it contains multiple functional domains that are required for coronavirus replication. Despite the numerous functional studies on MHV and its nsp3 domain, the structure of only one domain in nsp3, the small ubiquitin-like domain 1 (Ubl1), has been determined. We report here the x-ray structure of three tandemly linked domains of MHV nsp3, including the papain-like protease 2 (PLP2) catalytic domain, the ubiquitin-like domain 2 (Ubl2), and a third domain that we call the DPUP (domain preceding Ubl2 and PLP2) domain. DPUP has close structural similarity to the severe acute respiratory syndrome coronavirus unique domain C (SUD-C), suggesting that this domain may not be unique to the severe acute respiratory syndrome coronavirus. The PLP2 catalytic domain was found to have both deubiquitinating and deISGylating isopeptidase activities in addition to proteolytic activity. A computationally derived model of MHV PLP2 bound to ubiquitin was generated, and the potential interactions between ubiquitin and PLP2 were probed by site-directed mutagenesis. These studies extend substantially our structural knowledge of MHV nsp3, providing a platform for

further investigation of the role of nsp3 domains in MHV viral replication.

Coronaviruses (CoVs)<sup>3</sup> are enveloped positive-sense RNA viruses, with the largest genomes (25.5–32 kb) among known RNA viruses. CoVs can infect a variety of species, including animals and humans, causing respiratory and gastrointestinal illnesses (1). Physiological consequences of human infection by CoVs are usually mild, except in immunocompromised individuals, where the outcome can be much more severe and even lead to death (1). However, emerging CoVs are capable of being extremely pathogenic. The most serious epidemic caused by an emerging human coronavirus (HCoVs) occurred in 2002–2003, when the global outbreak of severe acute respiratory syndrome (SARS), caused by SARS-CoV, resulted in a case fatality rate of ~10% (2). Although a decade has passed since the outbreak of SARS, no drugs or vaccines are approved for the treatment of coronaviral infections. The emergence of a novel coronavirus in 2012, the Middle East respiratory syndrome coronavirus (MERS-CoV), which has a case fatality rate of ~38% (3), highlights the need for the discovery of antiviral drugs and/or vaccines against infections caused by CoVs.

Studies of MERS-CoV suggest that, similar to SARS-CoV, the new coronaviral species originates from an animal reservoir (4–6). The zoonotic nature of HCoVs makes future reemergence of coronaviral global epidemics, such as SARS and MERS, a potential threat to human health. In addition, porcine epidemic diarrhea virus is a coronavirus that has devastated the porcine industry worldwide. The outbreak of porcine epidemic

\* This work was supported, in whole or in part, by National Institutes of Health, NIAID, Grant R01 AI085089 (to A. D. M. and S. C. B.). Crystallization and DNA sequencing were supported in part by the Purdue Center for Cancer Research Macromolecular Crystallography and DNA Sequencing Shared Resources, which are supported by National Institutes of Health Grant P30 CA023168. Use of the Advanced Photon Source, an Office of Science User Facility operated for the United States Department of Energy Office of Science by Argonne National Laboratory, was supported by the Department of Energy under Contract DE-AC02-06CH11357. Use of the Life Science-Collaborative Access Team Sector 21 was supported by the Michigan Economic Development Corporation and the Michigan Technology Tri-Corridor (Grant 085P1000817). The authors declare that they have no conflicts of interest with the contents of this article.

The atomic coordinates and structure factors (code 4YPT) have been deposited in the Protein Data Bank (<http://www.pdb.org/>).

<sup>1</sup> Present address: Dept. of Biochemistry and Molecular Biology, University of Massachusetts Amherst, Amherst, MA 01002.

<sup>2</sup> Supported in part by the Walther Cancer Foundation. To whom correspondence should be addressed. Tel.: 765-494-1924; Fax: 765-496-1189; E-mail: amesecar@purdue.edu.

<sup>3</sup> The abbreviations used are: CoV, Coronavirus; HCoV, human coronavirus; SARS, severe acute respiratory syndrome; MERS, Middle East respiratory syndrome; MHV, murine hepatitis virus; TGEV, transmissible gastroenteritis virus; PLP or PLP<sub>pro</sub>, papain-like protease; nsp, non-structural protein; SUD, severe acute respiratory syndrome coronavirus unique domain; DUB, deubiquitinating; SeMet, selenomethionine; AMC, 7-amino-4-methylcoumarin; Ub, ubiquitin; Ubl, ubiquitin-like; BisTris, 2-[bis(2-hydroxyethyl)amino]-2-(hydroxymethyl)propane-1,3-diol; PDB, Protein Data Bank; aa, amino acids.

## Structure of Three Tandemly Linked Domains of MHV nsp3

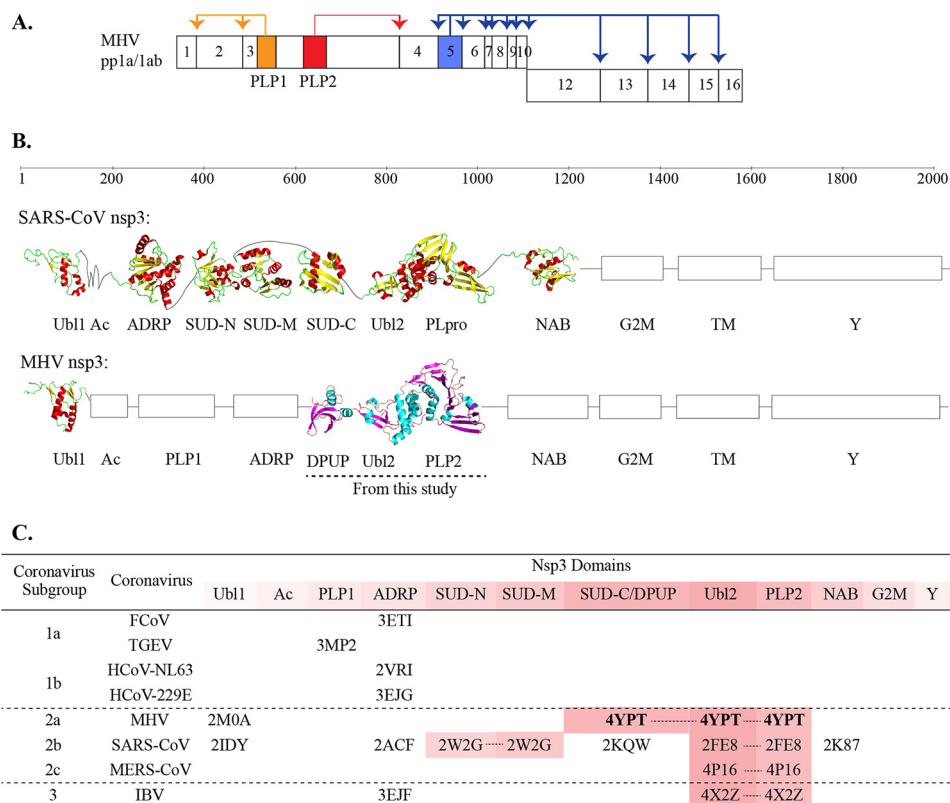


**FIGURE 1. Domain organization of the MHV and SARS-CoV coronavirus polyprotein and nsp3.** *A*, domain organization of the MHV polyprotein. The locations of the different nsps resulting from the processing of polyproteins are numbered 1–16. The two papain-like protease domains of MHV within nsp3, PLP1 and PLP2, are represented in orange and red, respectively, whereas the 3C-like protease (3CLpro) within nsp5 is represented in blue. The corresponding cleavage sites for each protease (PLP1, PLP2, and 3CLpro) are indicated by arrows and are colored according to the protease that performs the cleavage. *B*, domain architecture of SARS-CoV nsp3 in comparison with MHV nsp3. Domains with known structures are shown as ribbons, whereas domains with unknown structures are represented as boxes. For SARS-CoV, only one PLpro is encoded in nsp3, and it catalyzes cleavage of the polyprotein at all three cleavage sites. The structures of the three MHV nsp3 domains determined in this study are underscored with dashed lines. PDB codes are as follows: SARS-CoV nsp3, 2IDY, 2ACF, 2W2G, 2KQW, 2FE8, and 2K87; MHV nsp3, 2M0A and 4YPT (from this study). *C*, a summary of the currently known structures of various nsp3 domains within CoVs studied to date (13–18, 22, 30, 53, 54, 63, 64). The currently known nsp3 domains are indicated at the top and are shaded in different shades of red. The PDB codes for the structures of individual or single domains are listed under the domain acronym. The PDB codes for the structures of domains that have been determined from a single polypeptide chain are connected with dashed lines and are shaded according to the color code of the corresponding domains.

diarrhea virus in the United States in 2013/2014 killed over 7 million pigs and resulted in significant economic loss (7). Therefore, a better understanding of the replication and pathogenesis of CoVs is urgently needed to develop effective treatments against coronaviral infections.

Murine hepatitis virus (MHV) is a member in the  $\beta$ -coronavirus genogroup 2a, which has long served as a model system for the study of CoVs. The first two-thirds of the giant coronavirus genome contains two overlapping open reading frames, ORF1a and ORF1b. They encode two viral replicase polyproteins, pp1a from ORF1a and pp1ab that results from a  $-1$  frameshift between ORF1a and ORF1b (Fig. 1A). The polyproteins are then processed by viral papain-like proteases (PLPs) and a 3C-like protease (3CL<sup>pro</sup> or nsp5) into 16 non-structural proteins (nsps) that are involved in the assembly of double-membrane vehicles, essential for viral RNA replication (8–11).

Among the 16 nsps, nsp3 is the largest replicase subunit, and it contains several domains of functional and structural importance for virus replication (12). Nsp3 of SARS-CoV has been well studied, with two-thirds of nsp3 having been characterized structurally by either x-ray crystallography or NMR (Fig. 1, B and C) (13–18). In contrast, there is a paucity of structural information of MHV nsp3. Extensive functional studies of

domains within MHV nsp3 have been conducted, but little structural information on these domains is currently available (Fig. 1, B and C) (19–23). In fact, with the exception of SARS-CoV, the structural information of most CoVs' nsp3 is still missing (Fig. 1C). Interestingly, the SARS-unique domain (SUD), which consists of three domains, the N-terminal domain (SUD-N), the middle domain (SUD-M), and the C-terminal domain (SUD-C), has been identified within SARS-CoV nsp3 (16). It was originally proposed that the SUD domain is unique to only SARS and bat CoVs within the  $\beta$ -coronavirus genogroups 2b and 2c (12). However, in this study, we present structural evidence that this is not the case because the SUD-C appears to also exist in MHV.

The PLP domains within nsp3 are responsible for proteolytic processing of the N-terminal polyprotein (Fig. 1A). In addition to the proteolytic activity, several coronaviral PLPs have been shown to possess deubiquitinating (DUB) activity (25–31, 65). Moreover, SARS-CoV papain-like protease (PLpro), MERS-CoV PLpro, and HCoV-NL63 PLP2 have also been shown to have delISGylating activity (25, 29, 32, 33), which removes ISG15 (interferon-stimulated gene 15, a ubiquitin-like molecule) from proteins, possibly counteracting the antiviral state

triggered by ISG15 conjugation (34). Because ubiquitination and ISGylation are known to play important roles in the regulation of numerous cellular pathways, including innate immune responses, it has been proposed that the CoVs may employ the DUB and deISGylating activities of PLPs to antagonize host innate immune responses to infection. Indeed, both SARS-CoV PLpro and HCoV-NL63 PLP2 have been shown to interfere with the IRF3 and NF- $\kappa$ B signaling pathways for interferon (IFN) production (33, 35). We also recently demonstrated that infection of  $\alpha/\beta$  interferon receptor knock-out (IFNAR(-/-)) mice with a chimeric Sindbis virus harboring SARS-CoV PLpro and ISG15 expression genes suppresses ISG15-mediated protection during viral infection (36). Most recently, it was discovered that MERS-CoV PLpro displays IFN antagonism activity (25, 29, 37). MHV PLP2 has also been shown to inhibit cellular type I interferon production by deubiquitinating TBK1 (TANK-binding kinase-1) (38, 39). However, the ability of purified MHV PLP2 enzyme to remove ubiquitin and ISG15 from substrates has not yet been demonstrated (see below).

Here we disclose the first x-ray crystal structure of the MHV PLP2 catalytic domain and two of its adjacent domains within nsp3. For clarity, this construct of PLP2 will be referred to as PLP2+ throughout this work. Kinetic characterization of recombinant MHV PLP2+ reveals that PLP2+ possesses both deubiquitinating and deISGylating activities. We present a computationally derived model of PLP2 in complex with ubiquitin aldehyde (Ubal), based on our recently reported structure of SARS-CoV PLpro in complex with Ubal (40) to gain insights into the molecular interactions between PLP2 and Ub, and these interactions are probed via mutagenesis and cell culture studies.

## Experimental Procedures

**Constructs of PLP2+ for Expression**—The construct (pEV-L8-PLP2+, polyprotein aa 1525–1911 with the accession number P0C6V0 cloned into pEV-L8 vector) used for the expression of PLP2+ in *Escherichia coli* cells was the same as described previously (23). Constructs for PLP2+ mutants (D1772R, D1807R, Y1824F, Y1824A, and F1812A) were generated by site-directed mutagenesis following the QuikChange protocol (Stratagene) with minor temperature cycling modifications to maximize the yield of the PCR products. The introduced mutations were then verified by DNA sequencing of the entire insert.

**Expression and Purification of PLP2+**—The expression and purification of PLP2+ followed the procedure described previously (23). Purified PLP2+ was concentrated to 12 mg/ml for protein crystallization or flash-frozen in the same buffer with the addition of glycerol to a final concentration of 2% using liquid nitrogen. The final frozen enzyme was stored at  $-80^{\circ}\text{C}$ .

To express selenomethionine (SeMet)-substituted PLP2+, pEV-L8-PLP2+ was transformed into *E. coli* strain B834 cells. Two liters of cells were grown in M9 medium (supplemented with thiamine, trace metal mix, L-SeMet, and all amino acids except unlabeled methionine) at  $37^{\circ}\text{C}$  until the  $A_{600}$  reached 0.6. At this point, protein expression was induced by the addition of isopropyl 1-thio- $\beta$ -D-galactopyranoside to a final concentration of 1 mM, and the cells were grown overnight at  $18^{\circ}\text{C}$  with constant shaking. The procedure for purification of SeMet

PLP2+ was the same as described previously for wild-type, unlabeled PLP2+ (23).

Expression of PLP2+ mutants followed the procedure for WT PLP2+, except the induction with 0.1 mM isopropyl 1-thio- $\beta$ -D-galactopyranoside was performed at  $18^{\circ}\text{C}$  for overnight instead of at  $25^{\circ}\text{C}$  for 6 h. The PLP2+ mutants along with WT PLP2+ as a control were purified through one-step immobilized metal affinity chromatography using separate 20-ml gravity columns (Bio-Rad) packed with 2 ml of nickel-nitrilotriacetic acid resin (Thermo Scientific) for each protein. Briefly, the cell pellet from 500 ml of culture (the weight of cell pellet varies between mutants, ranging from 1.2 to 2 g) was resuspended in 40 ml of Buffer A (25 mM Tris, pH 7.0, 500 mM NaCl, 20 mM imidazole, 5 mM  $\beta$ -mercaptoethanol) supplemented with lysozyme and DNase I. Cells were then lysed by sonication and clarified with centrifugation following the procedures described previously (23). Clarified lysate was next loaded onto the column pre-equilibrated with Buffer A. Unbound proteins were washed with 20 column volumes of Buffer A, and bound proteins were then eluted with 7 ml of 100% Buffer B (25 mM Tris, pH 7.0, 500 mM NaCl, 500 mM imidazole, 5 mM  $\beta$ -mercaptoethanol). Eluted samples were then dialyzed in Buffer C (50 mM HEPES, pH 7.0, 100 mM NaCl, 5 mM  $\beta$ -mercaptoethanol) at  $4^{\circ}\text{C}$  overnight. The resulting proteins were then used for further activity characterization.

Throughout the protein purification, the specific activity of PLP2+ was determined using a 50  $\mu\text{M}$  concentration of the Z-RLRGG-AMC substrate following the procedure described below. The concentration of PLP2+ during the purification was measured through the cuvette-based Bio-Rad Bradford protein assay.

**Steady-state Kinetic Studies of PLP2+**—The substrate Z-RLRGG-AMC, where Z is the carboxybenzyl protecting group and RLRGG is the C-terminal peptide of Ub and ISG15, was purchased from BaChem, whereas Ub-AMC and ISG15-AMC were purchased from Boston Biochem. In each of these substrates, AMC represents 7-amino-4-methylcoumarin. Ub-AMC and ISG15-AMC assays were performed at  $25^{\circ}\text{C}$  in triplicate in a final volume of 50  $\mu\text{l}$ , whereas the Z-RLRGG-AMC assay was performed at  $25^{\circ}\text{C}$  in triplicate in a final volume of 100  $\mu\text{l}$ . Assay buffer contained 50 mM HEPES, pH 7.0, 0.1 mg/ml bovine serum albumin (BSA), and 2 mM DTT. Assays were initiated by the addition of enzymes. The final enzyme concentrations were as follows for each assay: 3  $\mu\text{M}$  for the Z-RLRGG-AMC assay, 5 nM for the Ub-AMC assay, and 10 nM for the ISG15-AMC assay. Rates of hydrolysis of the substrates by PLP2+ were monitored by recording the increase in fluorescence intensity of the released AMC group (excitation  $\lambda$ ,  $340 \pm 8$  nm; emission  $\lambda$ ,  $460 \pm 8$  nm) as a function of time using an EnVision multimode plate reader from PerkinElmer Life Sciences. The initial slope of the reaction in units of fluorescence per unit time (arbitrary fluorescence units/min) was converted to the amount of product produced per unit time ( $\mu\text{M}/\text{min}$ ) using the extinction coefficient of the product (arbitrary fluorescence units/ $\mu\text{M}$ ) determined following the procedure as described in (25). For the Ub-AMC substrate, the initial velocities were plotted against Ub-AMC concentrations, and the data were fit to the Michaelis-Menten equation,  $v/[E] = k_{\text{cat}}[S]/$

## Structure of Three Tandemly Linked Domains of MHV nsp3

( $K_m + [S]$ ), where  $v$  is the initial velocity ( $\mu\text{M}/\text{min}$ ),  $[E]$  is the enzyme concentration ( $\mu\text{M}$ ),  $k_{\text{cat}}$  is the turnover number in reciprocal minutes ( $\text{min}^{-1}$ ) and represents the maximum number of substrate molecules converted to products/enzyme molecule/min,  $[S]$  is the substrate concentration, and  $K_m$  is the substrate concentration ( $\mu\text{M}$ ) at which the reaction rate is half-maximum. For the substrates ISG15-AMC and Z-RLRGG-AMC, where no saturation of the enzyme was observed, plots of initial velocities *versus* substrate concentrations were fit to the equation,  $v/[E] = k_{\text{app}}[S]$ , where  $k_{\text{app}}$  represents the apparent rate constant ( $k_{\text{cat}}/K_m$ ) in units of  $\mu\text{M}^{-1} \text{min}^{-1}$ . When  $[S] \ll K_m$ ,  $k_{\text{app}}$  approximates  $k_{\text{cat}}/K_m$ .

**Activity Characterization of PLP2+ Mutants**—The kinetic activity of each PLP2+ mutant was measured in the presence of 50  $\mu\text{M}$  Z-RLRGG-AMC or 500 nM Ub-AMC following the procedures described above. The initial rates of each reaction were then determined and compared directly to the value for WT PLP2+ at the same substrate concentration.

**Ubiquitin Chain Cleavage Assay**—A diubiquitin (di-Ub) panel including all eight ubiquitin linkage types (Lys<sup>6</sup>, Lys<sup>11</sup>, Lys<sup>27</sup>, Lys<sup>29</sup>, Lys<sup>33</sup>, Lys<sup>48</sup>, Lys<sup>63</sup>, and linear), Lys<sup>48</sup>-linked tetraubiquitin, and Lys<sup>63</sup>-linked hexaubiquitin were purchased from Boston Biochem. Ubiquitin chain-cleaving reactions were performed by incubating a 2  $\mu\text{M}$  concentration of each ubiquitin chain listed above with a 20 nM concentration of recombinant PLP2+ in buffer (50 mM HEPES, pH 7.0, 100 mM NaCl, 0.1 mg/ml BSA, and 2 mM DTT) at 25 °C for various times ranging from 5 min to 2 h. At the end of each time period, except for the panel of di-Ub substrates, where only one time point was taken at 2 h, the reactions were quenched by the addition of NuPAGE LDS sample buffer (Invitrogen). As a control, the same amount of ubiquitin chains was incubated at 25 °C without any enzyme. Samples were then analyzed by SDS-PAGE using NuPAGE Novex 4–12% BisTris mini gels (Invitrogen).

**Protein Crystallization**—Initial crystallization conditions for MHV PLP2+ were first identified after performing a high-throughput crystallization screen using a series of commercial crystallization screens from Qiagen. Briefly, 1  $\mu\text{l}$  of purified MHV PLP2+ at three concentrations (6, 12, and 24 mg/ml) was pipetted into the three subwells of a 96-3 well sitting drop plate (Greiner CrystalQuick crystallization plate), and 1  $\mu\text{l}$  of reservoir solution was then added to the drop. The plates were then incubated at 20 °C. An initial crystallization hit was identified after 2 days of growth in a solution containing 100 mM HEPES, pH 7.5, 2% PEG 400, and 2 M  $(\text{NH}_4)_2\text{SO}_4$ . Initial crystals were small, with the longest dimension only 0.05 mm. Further optimization of the crystallization conditions was then carried out manually using 24-well sitting drop plates at 20 °C using a fine grid of 100 mM HEPES between pH 6.8 and pH 8.3 and PLP2+ microseeds of serial dilutions between  $10^4$  and  $10^{10}$ . Microseeds of PLP2+ were prepared by adding a crystallization drop (from a plate set up previously without the addition of microseeds) containing an abundance of small PLP2+ crystals to 20  $\mu\text{l}$  of the corresponding reservoir solution followed by serial dilutions in the same reservoir solution. To set up the crystallization plate, 2  $\mu\text{l}$  of purified PLP2+ at 6 mg/ml was pipetted into the subwell of the plate. To the subwell, 0.5  $\mu\text{l}$  of reservoir solution and 0.5  $\mu\text{l}$  of fresh prepared PLP2+ microseeds were

then added. Diffraction quality PLP2+ crystals grew within 2 days with dimensions of  $\sim 0.09$  by 0.12 mm. The optimal crystallization condition consisted of 100 mM HEPES, pH 8.0, 4% PEG 400, 2 M  $(\text{NH}_4)_2\text{SO}_4$ , and 5 mM DTT. SeMet PLP2+ was crystallized in the same way as unlabeled PLP2+.

**Data Collection and Structure Determination**—Crystals of MHV PLP2+ were harvested using nylon loops and then placed into reservoir solution supplemented with 20% glycerol for seconds before they were mounted to nylon loops by flash-cooling in liquid nitrogen. Crystals were then stored in a Dewar under liquid nitrogen until data collection. For data collection, cryo-cooled crystals were mounted under a stream of dry  $\text{N}_2$  at 100 K. One native data set and one SeMet peak data set were collected at the National Institutes of General Medical Sciences and Cancer 23-ID-B and Life Science-Collaborative Access Team 21-ID-D beamlines, respectively, at the Advanced Photon Source Synchrotron, Argonne National Laboratory. Both data sets were processed and scaled using HKL2000 (41). The native data set and the SeMet peak data set were processed and scaled to 2.60 and 2.80 Å, respectively. Initial phases were determined through the single-wavelength anomalous dispersion method using the SeMet peak data set. An initial model of PLP2+ was generated using the AutoSol module in Phenix (42). Phases were then further extended using the 2.60 Å native data set. However, the initial model resulting from AutoSol was incomplete because the first 90 residues at the N terminus were not built by the program. Through the iteration of manual model building in Coot (43), structure refinement with Phenix Refine (44), and automatic model building in ARP/wARP (45), the majority of the missing residues were built. The improved model was then further refined using Phenix Refine. Data collection and refinement statistics are shown in Table 2. Figures were generated using PyMOL (66).

**Generation of a Structure Model for MHV PLP2 Bound with Ubiquitin-Aldehyde**—The x-ray crystal structure of SARS-CoV PLpro in complex with ubiquitin-aldehyde (Ubal) (Protein Data Bank (PDB) code 4MM3) was used as a template to generate a model of MHV PLP2-Ub complex (40). Because the Ub structure could not be embedded directly into the ubiquitin binding site of the unliganded structure of MHV PLP2 without severe clashes with the fingertip region (the region in the fingers domain where the zinc atom coordinates to the four cysteine residues), we subjected the crystal structure determined in this study to a 1.2-ns isothermal (300 K) molecular dynamics simulation with explicit water molecules and NaCl ions (150 mM) (Desmond Molecular Dynamics System, Schrödinger, LLC). Remarkably, the trajectory of the simulation indicated an immediate opening of the “collapsed” fingertip region of MHV PLP2 beyond the positions observed in various liganded and unliganded SARS-CoV PLpro structures, as judged by the distance between the zinc atom and C $\alpha$  carbon of the active site catalytic cysteine. Subsequently, the zinc ion and the associated fingertip oscillated between open and collapsed states with decreasing amplitude. Next, we identified a conformational state that is the most similar to the one found in the SARS-CoV PLpro-Ubal complex and used it to generate a structural model of a MHV PLP2-Ubal complex. The preliminary model was refined further by a secondary molecular dynamics simulation

TABLE 1

Kinetic parameters of MHV PLP2+ with substrates RLRGG-AMC, Ub-AMC, and ISG15-AMC in comparison with SARS-CoV PLpro and MERS-CoV PLpro

	Substrate		
	RLRGG-AMC	Ub-AMC	ISG15-AMC
<b>MHV PLP2+</b>			
$k_{\text{cat}}/K_m$ ( $\mu\text{M}^{-1} \text{min}^{-1}$ )	0.0016 <sup>a</sup>	38.3 ± 6.3	2.3 ± 0.1 <sup>a</sup>
$k_{\text{cat}}$ ( $\text{min}^{-1}$ )		49.8 ± 2.9	
$K_m$ ( $\mu\text{M}$ )		1.3 ± 0.2	
<b>SARS-CoV PLpro<sup>b</sup></b>			
$k_{\text{cat}}/K_m$ ( $\mu\text{M}^{-1} \text{min}^{-1}$ )	0.3 ± 0.1 <sup>a</sup>	1.5 ± 0.3	28.9 ± 5.3
$k_{\text{cat}}$ ( $\text{min}^{-1}$ )		75.9 ± 8.1	436 ± 40
$K_m$ ( $\mu\text{M}$ )		50.6 ± 7.4	15.1 ± 2.4
<b>MERS-CoV PLpro<sup>b</sup></b>			
$k_{\text{cat}}/K_m$ ( $\mu\text{M}^{-1} \text{min}^{-1}$ )	0.003 <sup>a</sup>	1.3 ± 0.2	9.9 ± 1.6
$k_{\text{cat}}$ ( $\text{min}^{-1}$ )		18.8 ± 1.2	32.6 ± 1.8
$K_m$ ( $\mu\text{M}$ )		14.3 ± 2.0	3.3 ± 0.5

<sup>a</sup> For non-saturating substrates,  $k_{\text{app}}$  is calculated to approximate  $k_{\text{cat}}/K_m$ .

<sup>b</sup> The kinetic parameters of SARS-CoV PLpro and MERS-CoV PLpro are from Baez-Santos *et al.* (25).

of a non-covalent complex to allow for extra flexibility at the C terminus of Ub, which produced a number of structurally similar conformational states. A state with optimal interaction energetics, characterized by a comparatively high number of hydrogen-bonding, hydrophobic, and favorable electrostatic contacts was used as the complex model thereafter. The persistence of the interactions between PLP2 and Ubal during the simulation was calculated. For comparison, the structure of the SARS-CoV PLpro-Ubal complex was also subject to a 1.2-ns molecular dynamics simulation.

**Luciferase Reporter Assay**—The luciferase assay followed the procedure described previously (25). HEK293T cells were transfected using 50 ng of *Renilla* luciferase, 100 ng of IFN- $\beta$ -luc, and the indicated PLP expression plasmids described previously (23). 50 ng of N-RIG-I/well was transfected for simulation.

## Results

**Substrate Specificity of MHV PLP2+**—The MHV PLP2+ catalytic core (pp1ab residues 1668–1911) with a flanking N-terminal domain (pp1a residues 1525–1607) and the Ubl2 domains (pp1ab residues 1608–1667) was expressed and purified from *E. coli*. The final purified protein is a 389-amino acid protein (43.5 kDa), with two additional residues at the N terminus resulting from removal of the octahistidine tag after tobacco etch virus protease cleavage. Herein, we refer to this three-domain protein construct from nsp3 as PLP2+ for simplicity.

Kinetic characterization of PLP2+ was performed with three different fluorogenic substrates, Ub-AMC, ISG15-AMC, and Z-RLRGG-AMC. These three substrates were used to measure the deubiquitinating, deISGylating, and proteolytic activities of PLP2+. Plots of initial rates *versus* increasing concentrations of either Z-RLRGG-AMC or ISG15-AMC up to the highest substrate concentrations tested show no signs of substrate saturation (data not shown). Therefore, data were fit to a line to derive the apparent rate constant,  $k_{\text{cat}}/K_m$ , from the slopes (Table 1). On the other hand, PLP2+ is readily saturated by the substrate Ub-AMC, so data were fit to the Michaelis-Menten equation, resulting in a  $K_m$  value of  $1.3 \pm 0.2 \mu\text{M}$  and a  $k_{\text{cat}}$  value of  $49.8 \pm$

$2.9 \text{ min}^{-1}$ . The resulting kinetic parameters for the PLP2+ catalyzed hydrolysis of all three substrates are summarized in Table 1, where they are compared with the kinetic parameters of SARS-CoV PLpro and MERS-CoV PLpro, which were determined previously (25).

Based on the apparent  $k_{\text{cat}}/K_m$  values, MHV PLP2+ catalyzes the hydrolysis of Ub-AMC  $\sim 17$ -fold more efficiently than ISG15-AMC and 24,000-fold more efficiently than Z-RLRGG-AMC. This order of substrate preference for MHV PLP2+ (Ub-AMC > ISG15-AMC  $\gg$  Z-RLRGG-AMC) stands in contrast to the SARS-CoV and MERS-CoV PLpro enzymes, which prefer ISG15-AMC over Ub-AMC by about 19- and 8-fold, respectively (Table 1). Both SARS-CoV and MERS-CoV PLpro also highly prefer ISG15-AMC by 96- and 3,300-fold over the Z-RLRGG-AMC substrate. The significant difference between the PLP2+ and PLpro-mediated hydrolysis of Ub-AMC or ISG15-AMC and Z-RLRGG-AMC suggests that there are additional and important interactions between PLP2 and Ub outside of the enzyme's catalytic center (*i.e.* beyond the reactive cysteine and  $S_5$ – $S_1$  substrate recognition subsites).

The ability of PLP2+ to act as deubiquitinating enzyme and catalyze the hydrolysis of isopeptide bonds was explored next by testing its specificity toward ubiquitin chains. Di-Ubs with different isopeptide linkages (Lys<sup>6</sup>, Lys<sup>11</sup>, Lys<sup>27</sup>, Lys<sup>29</sup>, Lys<sup>33</sup>, Lys<sup>48</sup>, or Lys<sup>63</sup>) or a peptide linkage (linear Ub) were incubated with PLP2+, and the reaction products were analyzed by SDS-PAGE (Fig. 2A). The results show that MHV PLP2+ is capable of cleaving all diubiquitins with isopeptide bonds into monoubiquitins but not linear-Ub, which contains a peptide bond (Fig. 2A). In addition, the efficiency of diubiquitin cleavage by PLP2+ appears to be linkage-dependent because hydrolyses of Lys<sup>11</sup>-, Lys<sup>48</sup>- and Lys<sup>63</sup>-linked di-Ubs are the most efficient. After 2 h, these di-Ubs have been completely processed to mono-Ub, whereas unreacted substrate still remains for Lys<sup>6</sup>-, Lys<sup>27</sup>-, Lys<sup>29</sup>-, and Lys<sup>33</sup>-linked di-Ubs.

Because Lys<sup>48</sup>- and Lys<sup>63</sup>-linked polyubiquitin chains are the most characterized chain types and the most ubiquitous in cell signaling pathways, we determined the time course for hydrolysis of Lys<sup>48</sup>-linked tetraubiquitin (Lys<sup>48</sup>-Ub<sub>4</sub>) and Lys<sup>63</sup>-linked hexaubiquitin (Lys<sup>63</sup>-Ub<sub>6</sub>) by MHV PLP2+ (Fig. 2, B and C). The data show that PLP2+ processes Lys<sup>48</sup>-Ub<sub>4</sub> and Lys<sup>63</sup>-Ub<sub>6</sub> with similar catalytic efficiency.

**Crystallization and X-ray Structure Determination of MHV PLP2+**—Purified MHV PLP2+ was readily crystallized by the microseeding approach from a solution containing  $\sim 6$  mg/ml enzyme in crystallization solution (100 mM HEPES, pH 8.0, 4% PEG 400, 2 M  $(\text{NH}_4)_2\text{SO}_4$ , and 5 mM DTT). A complete x-ray data set on a native crystal was collected to 2.60 Å resolution (Table 2). Multiple attempts to determine the structure of MHV PLP2+ through numerous molecular replacement approaches using the available SARS-CoV PLpro structures (PDB codes 2FE8, 3E9S, and 3MJ5) or the TGEV PLP1 structure (3MP2) proved unsuccessful. Therefore, experimental phasing using heavy atom derivatives and SeMet-substituted MHV PLP2+ was pursued. Ultimately, experimental phases were determined via the single-wavelength anomalous dispersion approach from a 2.80 Å data set collected from a SeMet-substituted MHV PLP2+ crystal. Both native and SeMet PLP2+ pro-

## Structure of Three Tandemly Linked Domains of MHV nsp3

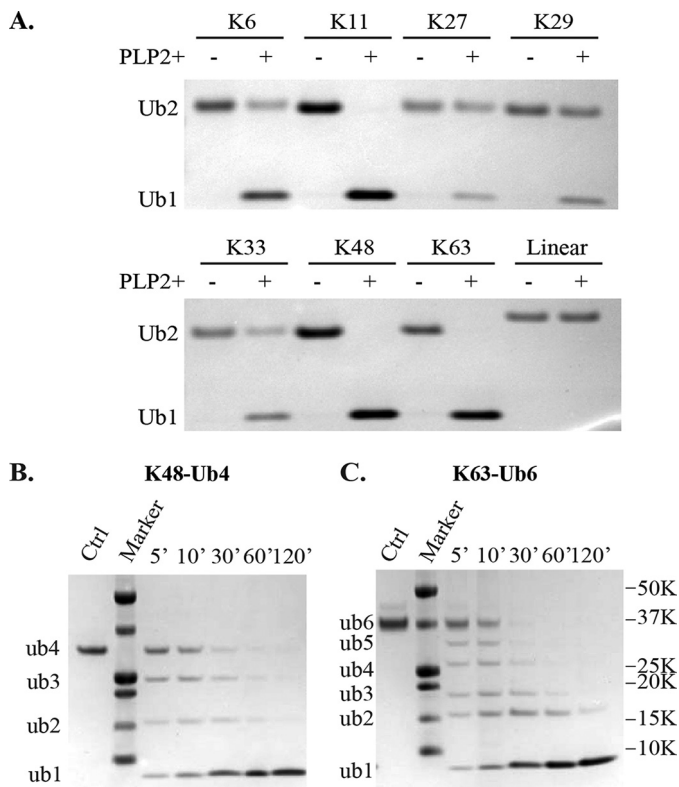


**FIGURE 2. PLP2+-mediated processing of ubiquitin chains.** *A*, survey of the hydrolysis of di-Ub by PLP2+. 0.5  $\mu$ g of di-Ub with different linkages (Lys<sup>6</sup>, Lys<sup>11</sup>, Lys<sup>27</sup>, Lys<sup>29</sup>, Lys<sup>33</sup>, Lys<sup>48</sup>, Lys<sup>63</sup>, and linear) was incubated at 25 °C with 20 nM PLP2+ for 2 h. Di-Ub incubated without PLP2+ serves as the negative control. *B* and *C*, time-dependent hydrolysis of Lys<sup>48</sup>-Ub4 (*B*) and Lys<sup>63</sup>-Ub6 (*C*) by PLP2+. The reactions were incubated at 25 °C, and aliquots were removed at five different time points, quenched with sample buffer, and then analyzed by SDS-PAGE. Polyubiquitin chains incubated without PLP2+ serve as negative control (*ctrl*). Markers were (from top to bottom) 50, 37, 25, 20, 15, and 10 kDa.

teins crystallized in the  $I2_13$  space group with one PLP2+ monomer in the asymmetric unit. Because PLP2+ was determined to be a monomer in solution based on size exclusion chromatography/multiangle light scattering analysis (data not shown), the asymmetric unit contains the biologically relevant monomer. The final structure was determined and refined against the native data set to a resolution of 2.60 Å with final  $R$ -values of  $R_{\text{work}} = 17.1\%$  and  $R_{\text{free}} = 22.1\%$ . The final x-ray data collection and refinement statistics are summarized in Table 2. The final MHV PLP2+ structural model had observable electron density for residues 1533–1910. The first 10 N-terminal and last C-terminal residues had weak or unobservable electron density.

**The X-ray Structure of MHV PLP2+ Reveals a DPUP Domain in MHV nsp3**—The crystal structure of the MHV PLP2 catalytic core and flanking N-terminal and Ubl2 domains consists of five domains: fingers, palm, thumb, Ubl2, and DPUP (Fig. 3A). The thumb, palm, and fingers domains form the catalytic core of PLP2, which has an architecture resembling a right hand. The thumb domain (aa 1668–1786 in the expression construct) is primarily made up of six helices ( $\alpha 4$ – $\alpha 9$ ), with two short anti-parallel strands ( $\beta 11$ – $\beta 12$ ) between helices  $\alpha 5$  and  $\alpha 6$ . The palm domain (aa 1842–1909) is formed by six anti-parallel strands ( $\beta 18$ – $\beta 23$ ). Finally, the fingers domain contains two short helices, one short strand, and one  $\beta$ -sheet consisting of

**TABLE 2**  
Data collection and refinement statistics

Values in parentheses are for the last (highest resolution) shell.

	SeMet	Native
<b>Data collection</b>		
Beamline	211D-D	231D-B
Wavelength (Å)	0.98	1.03
Space group	$I2_13$	$I2_13$
Unit cell dimensions		
$a, b, c$ (Å)	$a = b = c = 154.9$	$a = b = c = 155.6$
$\alpha, \beta, \gamma$ (degrees)	$\alpha = \beta = \gamma = 90$	$\alpha = \beta = \gamma = 90$
Resolution (Å)	50.00–2.80 (2.85–2.80)	50.00–2.60 (2.64–2.60)
No. of reflections observed	472,931	537,164
No. of unique reflections	15,419	19,350
$R_{\text{merge}}$ (%) <sup>a</sup>	7.9 (77.8)	5.7 (74.9)
$R_{\text{pim}}$ (%) <sup>b</sup>	4.6 (27.4)	1.9 (24.6)
$I/\sigma I$	21.9 (2.4)	38.2 (4.5)
Completeness (%)	98.8 (100.0)	99.7 (100.0)
Redundancy	5.8 (5.8)	10.2 (10.2)
<b>Phasing</b>		
Resolution (Å)	49.00–3.10 (3.21–3.10)	
Figure of merit	0.43	
Sites	5 Se	
<b>Refinement</b>		
Resolution range (Å)		49–2.60 (2.74–2.60)
No. of reflections in working set		18,388 (2612)
No. of reflections in test set		998 (136)
$R_{\text{work}}$ (%) <sup>c</sup>		17.1 (21.0)
$R_{\text{free}}$ (%) <sup>d</sup>		22.2 (28.5)
Wilson B factor (Å <sup>2</sup> )		30.9
Average B factor (Å <sup>2</sup> )		54.5
Root mean square deviation from ideal geometry		
Bond length (Å)		0.008
Bond angle (degrees)		1.138
Ramachandran plot		
Most favored (%)		95.0
Allowed (%)		4.2
Disallowed (%)		0.8

<sup>a</sup>  $R_{\text{merge}} = \frac{\sum_{hkl} \sum_i |I_i(hkl) - \langle I(hkl) \rangle|}{\sum_{hkl} \sum_i I_i(hkl)}$ , where  $I_i(hkl)$  is the intensity of a given reflection, and  $\langle I(hkl) \rangle$  is the mean intensity of symmetry-related reflections.

<sup>b</sup>  $R_{\text{pim}} = \frac{\sum_{hkl} \sqrt{(1/n - 1) \sum_i |I_i(hkl) - \langle I(hkl) \rangle|}}{\sum_{hkl} \sum_i I_i(hkl)}$ , where  $n$  is the multiplicity.  $R_{\text{pim}}$  is multiplicity-weighted  $R_{\text{merge}}$ .

<sup>c</sup>  $R_{\text{work}} = \frac{\sum_{hkl} |F_{\text{obs}}| - F_{\text{calc}}}{\sum_{hkl} F_{\text{obs}}}$ , where  $F_{\text{obs}}$  and  $F_{\text{calc}}$  are the observed and calculated structure factors, respectively.

<sup>d</sup>  $R_{\text{free}}$  was calculated using 5% of the data set chosen at random that was excluded from the refinement.

four anti-parallel twisted strands. At the tip of the fingers domain, four cysteines (Cys<sup>1794</sup>, Cys<sup>1796</sup>, Cys<sup>1828</sup>, and Cys<sup>1830</sup>) coordinate a metal ion in a tetrahedral geometry. The identity of the metal was determined to be zinc via a fluorescence energy scan at the zinc x-ray absorption edge (data not shown).

The MHV ubiquitin-like (Ubl2) domain (aa 1608–1667) is composed of a  $\beta$ -grasp fold (46). The Ubl1 domain was first identified in nsp3 after the determination of the x-ray structure of SARS-CoV PLpro (17). Subsequently, a second Ubl domain was identified in nsp3 after determination of the NMR structure of the first 183 residues of the SARS-CoV nsp3 N terminus (13). The Ubl domain associated with PLpros and PLP2 is now designated as Ubl2, and the N-terminal Ubl domain is now designated as Ubl1 because it comes first in the primary sequence.

The x-ray structure of PLP2+ also reveals an unpredicted domain at the N terminus of MHV PLP2 that is formed by 85 residues. The domain consists of two helices ( $\alpha 1$  and  $\alpha 2$ ) that are connected by five anti-parallel  $\beta$ -strands ( $\beta 1$ – $\beta 5$ ). A DALI search (47) of this unpredicted domain against the PDB identified the C domain of the SARS unique domain (SUD-C) as the top match, with a Z-score of 7.3. Structural superposition of this domain with the SUD-C domain, using the DaliLite server

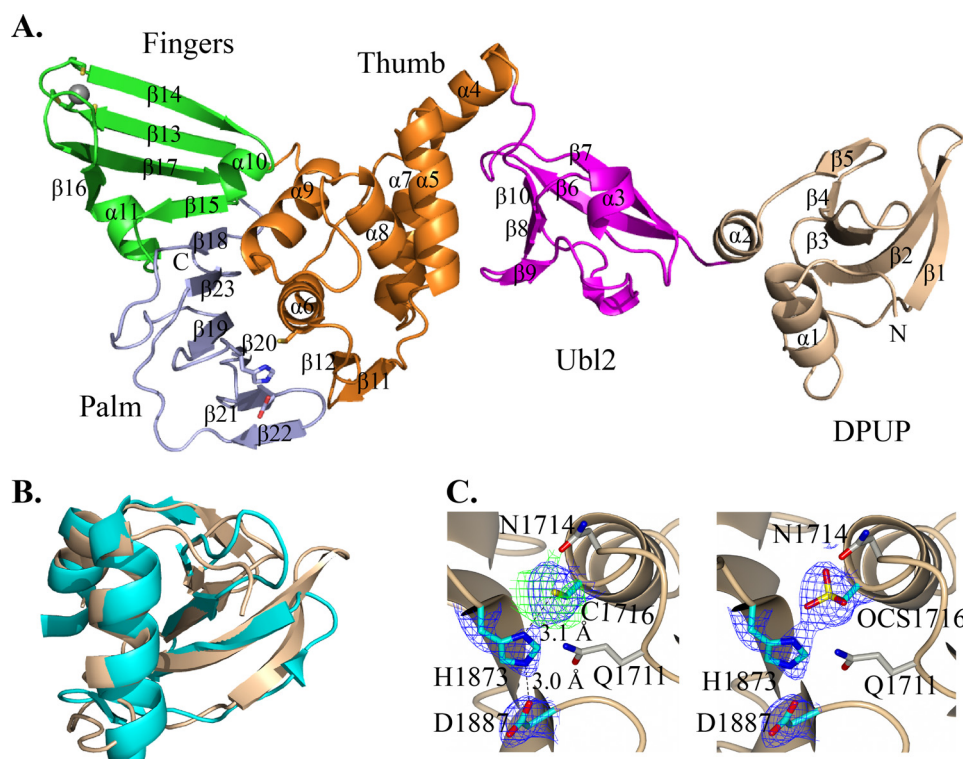


FIGURE 3. **X-ray crystal structure of PLP2+.** *A*, ribbon representation of the overall structure of PLP2+. The structure contains five domains: fingers (green), palm (light blue), thumb (orange), Ubl2 (magenta), and DPUP (wheat). The zinc atom in the fingertip of the fingers domain is shown as a gray sphere. The catalytic triad residues and the four zinc-coordinating cysteines from the fingers domain are represented as sticks. *B*, structural superposition of the DPUP domain (wheat) with SARS SUD-C domain (cyan; PDB code 2KQW). The root mean square deviation between the two structures is 2.1 Å over 63 aligned C $\alpha$  atoms at 13% sequence identity. *C*, electron density maps covering the catalytic triad before (left) and after (right) refinement of the sulfonic group at the catalytic Cys. In the right panel, the occupancies of the oxygen atoms in the sulfonic acid group were set to 0.5. In each panel, the residual electron density in  $F_o - F_c$  maps are colored green and are contoured at  $3\sigma$ , whereas the  $2F_o - F_c$  maps are colored blue and are contoured at  $1\sigma$ .

(48), shows that the root mean square deviation is 2.1 Å over 63 aligned backbone C $\alpha$  atoms, whereas the sequence identity is only 13% (Fig. 3*B*). Although the SUD has been proposed to be unique to SARS-CoV, the presence of this domain in MHV nsp3 calls into question its exclusivity (see “Discussion”). We designate this new domain in nsp3 as the DPUP (domain preceding Ubl2 and PLP2) domain because it does not engender exclusivity, and it allows for DPUP to be identified in other coronavirus nsp3s.

The active site of PLP2, which consists of a Cys<sup>1716</sup>-His<sup>1873</sup>-Asp<sup>1887</sup> catalytic triad, sits between the thumb and palm domains. Cys<sup>1716</sup> and Asp<sup>1887</sup> are both within hydrogen-bonding distance of His<sup>1873</sup> (3.1 and 3.0 Å, respectively; Fig. 3*C*), indicating that the active site is arranged in a catalytically competent manner, even in the absence of a substrate. Unlike SARS-CoV PLpro, where a tryptophan side chain forms part of the oxyanion hole (17), Gln<sup>1711</sup> occupies the same position in PLP2 and appears to be involved in the oxyanion hole stabilization (Fig. 3*C*). Asn<sup>1714</sup>, which is conserved among coronavirus PLPs, may also participate in stabilizing the oxyanion hole. Interestingly, after structural refinement of PLP2+, residual electron density surrounding the reactive cysteine (Cys<sup>1716</sup>) was observed, suggesting that it is partially oxidized to cysteic acid (Fig. 3*C*, left). X-ray refinement with a partially occupied cysteic acid was able to account for the residual electron density (Fig. 3*C*, right). Partial or complete oxidation of the catalytic cysteine is commonly observed in crystal structures of cysteine

proteases due to both the highly reactive nature of the side chain thiol group and its ability to coordinate thiophilic transition metals capable of oxidation (49). We have observed complete, partial, and no oxidation of the reactive cysteine in SARS-CoV PLpro x-ray structures (17, 50–52).

*Structural Comparison of MHV PLP2 to Known Structures of Coronavirus PLPs*—Prior to the structure of MHV PLP2, structures of other CoV PLPs, including SARS-CoV PLpro, MERS-CoV PLpro, TGEV PLP1, and IBV PLpro, have been determined (17, 30, 53, 54, 65) (Fig. 1). To help elucidate the function of coronavirus PLPs, the catalytic core of PLP2 was superimposed with the above known CoV PLP structures. The overall architectures of these proteins are similar, with root mean square deviation ranges from 1.7 Å (SARS-CoV PLpro, 218 of 242 aligned residues) to 2.8 Å (TGEV PLP1, 189 of 242 aligned residues). For the sake of clarity, only the structural superpositions of MHV PLP2 on SARS-CoV PLpro and MERS-CoV PLpro are shown (Fig. 4*A*). The Cys-His-Asp catalytic triads from these PLPs are well aligned (Fig. 4*B*). However, several differences in the structures are observed from the overlay. First, whereas the local geometry of the zinc-binding site is maintained in all these structures, the fingertip regions have different conformations and differing extents of opening/closure with respect to the palm domains. In contrast with SARS-CoV PLpro and MERS-CoV PLpro, the fingertip in PLP2 collapses toward the palm, rendering the canonical surface for ubiquitin binding too compact to accommodate the typical

## Structure of Three Tandemly Linked Domains of MHV nsp3

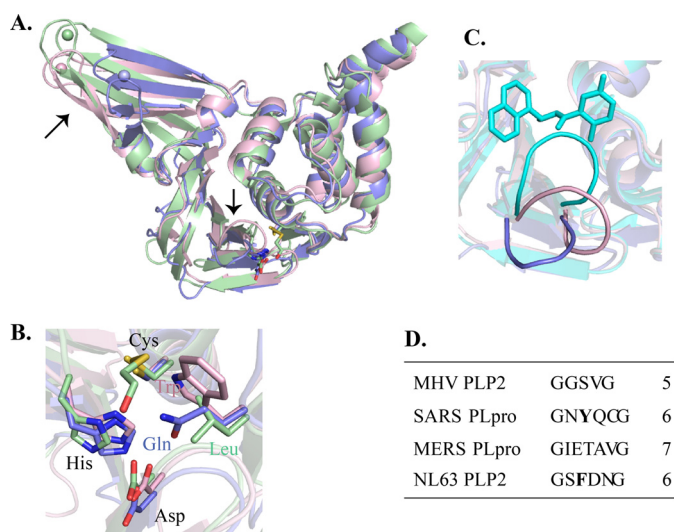


**FIGURE 4. Structural comparison among coronaviral PLPs.** *A*, structural superposition of unbound PLP2 (light blue), unbound SARS-CoV PLpro (light pink; PDB code 2FE8), and unbound MERS-CoV PLpro (light green; PDB code 4P16). Areas with major differences are indicated with black arrows. *B*, close-up view of the active site alignments. The Cys-His-Asp catalytic triad is conserved among the three proteins, whereas the oxanion hole residues are different. The color code is the same as in *A*. The catalytic cysteine in MERS-CoV PLpro was covalently modified by  $\beta$ -mercaptoethanol. *C*, conformations of the BL2 loops in different CoV PLPs. The color code is the same as in *A* with the additional structure of inhibitor-bound SARS-CoV PLpro shown in cyan (PDB code 3E9S). The loop from MERS-CoV PLpro is omitted because it is not visible in the structure. *D*, sequences of the BL2 loops in different CoV PLPs.

ubiquitin structure without some opening via conformational changes. Extensive flexibility within the fingers domain has been observed in the x-ray structure of the free enzyme form (*i.e.* with no substrates or ligands bound) of SARS-CoV PLpro, where an overlay of the three protomers within one asymmetric unit shows significant variations in the positions of the atoms in the fingers domain (up to 4.6 Å for zinc atoms) (17). The conformational flexibility of the fingers domain may regulate substrate binding and, hence, the activity of PLPs. However, given the tight packing of the crystal around the fingers domain (data not shown), there is the possibility that crystal packing may influence the conformation of the collapsed fingers domain in MHV PLP2.

Another region with significant differences among the PLPs is the  $L_{\beta 19-\beta 20}$  loop in PLP2 (sequence: <sup>1868</sup>GGSVG<sup>1872</sup>) (Fig. 4, *A* and *C*), referred to as the BL2 loop in ubiquitin-specific proteases. The length of the substrate loop varies in different CoVs (Figs. 4*D* and 6). Flanked with glycine residues, this loop is expected to be highly flexible. Indeed, this loop has been observed in different conformations in various structures of coronaviral PLPs (Fig. 4*C*). In the case of SARS-CoV PLpro, the loop (<sup>267</sup>GNYQCG<sup>272</sup>) is found in a closed arrangement when there is a bound inhibitor, whereas an open state is observed when the enzyme is crystallized as the free enzyme form (Fig. 4*C*). However, the loop in PLP2 is one residue shorter, and it is observed in an extended open conformation. Interestingly, the BL2 loop of PLP2 does not contain any phenylalanine or tyrosine residue. It has been shown for SARS-CoV PLpro and HCoV-NL63 PLP2 that having a phenylalanine or tyrosine on the BL2 loop is important for the binding of a series of potent PLP inhibitors (50, 52). On the other hand, MERS-CoV PLpro,

which does not have any phenylalanine or tyrosine residue on the BL2 loop, has no inhibition by these inhibitors (25). And our results have shown that MHV PLP2, which lacks a phenylalanine or tyrosine residue on the BL2 loop, is not affected by this series of inhibitors (data not shown).

**Potential Interactions between MHV PLP2 and Ubiquitin—** To gain insights into potential interactions between PLP2 and ubiquitin, we utilized the structure of the SARS-CoV PLpro-ubiquitin aldehyde (Ubal) complex (PDB code 4MM3) (40) as a template to generate a model of PLP2 in complex with Ubal via molecular dynamics (see “Experimental Procedures” for details). The resulting computational model of the MHV PLP2-Ubal complex reveals that the Ubal molecule is stabilized by numerous interactions at the canonical surface formed by the thumb-palm-fingers domains of PLP2, whereas the C-terminal residues of Ubal extend into the narrow opening of the active site, as expected. Henceforth, to differentiate the enzyme residues from Ub residues, the latter will be shown in italic type, whereas the former will be represented in normal type.

Extensive hydrogen-bonding interactions between the C-terminal residues of Ubal and the active site of PLP2 are observed in the model (Fig. 5*A*). This observation is consistent with the fact that PLP2 can hydrolyze the peptide substrate Z-RLRGG-AMC, albeit more than 20,000 times less efficiently than Ub-AMC. A similar network of hydrogen-bonding interactions has also been discovered in the structure of SARS-CoV PLpro-Ubal complex (Fig. 5*B*) (40). In SARS-CoV PLpro, the side chain of Tyr<sup>265</sup> interacts with the backbone of Arg<sup>74</sup> (Fig. 5*B*). A similar interaction is absent in PLP2 due to the substitution of Tyr<sup>265</sup> with Phe<sup>1866</sup>. However, the loss of this hydrogen-bonding interaction may not have a significant effect on the enzymatic activity because the Y265F mutant of SARS-CoV PLpro possesses activity comparable with that of WT (55). On the other hand, a potentially stable salt bridge interaction between the side chain of Arg<sup>74</sup> and Glu<sup>1766</sup> is observed in the PLP2-Ubal model (Fig. 5*A*). In the SARS-CoV PLpro-Ubal complex, however, a similar interaction is absent, as suggested by both the crystal structure (40, 55) and the 1.2-ns molecular dynamics analysis of the complex (data not shown). Overall, the differences in the interaction profiles between the C-terminal residues of Ubal and the active sites of MHV PLP2 and SARS-CoV PLpro do not adequately justify why the activity of PLP2 with Z-RLRGG-AMC is significantly lower than that of SARS-CoV PLpro. Perhaps the additional salt bridge between Glu<sup>1766</sup> and Arg<sup>74</sup> in the PLP2-Ubal model is detrimental to the activity of PLP2+ with Z-RLRGG-AMC because it could lead to substantial product inhibition. Alternatively, additional interactions that were not predicted by the molecular dynamics run may play an important role in the reduction of MHV PLP2+ activity against Z-RLRGG-AMC when compared with that of SARS-CoV PLpro.

In addition to the interactions near the active site, extensive contacts are predicted between MHV PLP2 and the Ubal core (residues 1–71) (Fig. 5*C*). Specifically, side chains of Tyr<sup>1824</sup> and Arg<sup>1803</sup> interact with the backbone carbonyl of Ala<sup>46</sup> through hydrogen bonding, whereas there is a backbone-backbone interaction between the amide of Phe<sup>1812</sup> and the carbonyl of Gly<sup>47</sup>. In addition, the side chain of Phe<sup>1812</sup> interacts with the



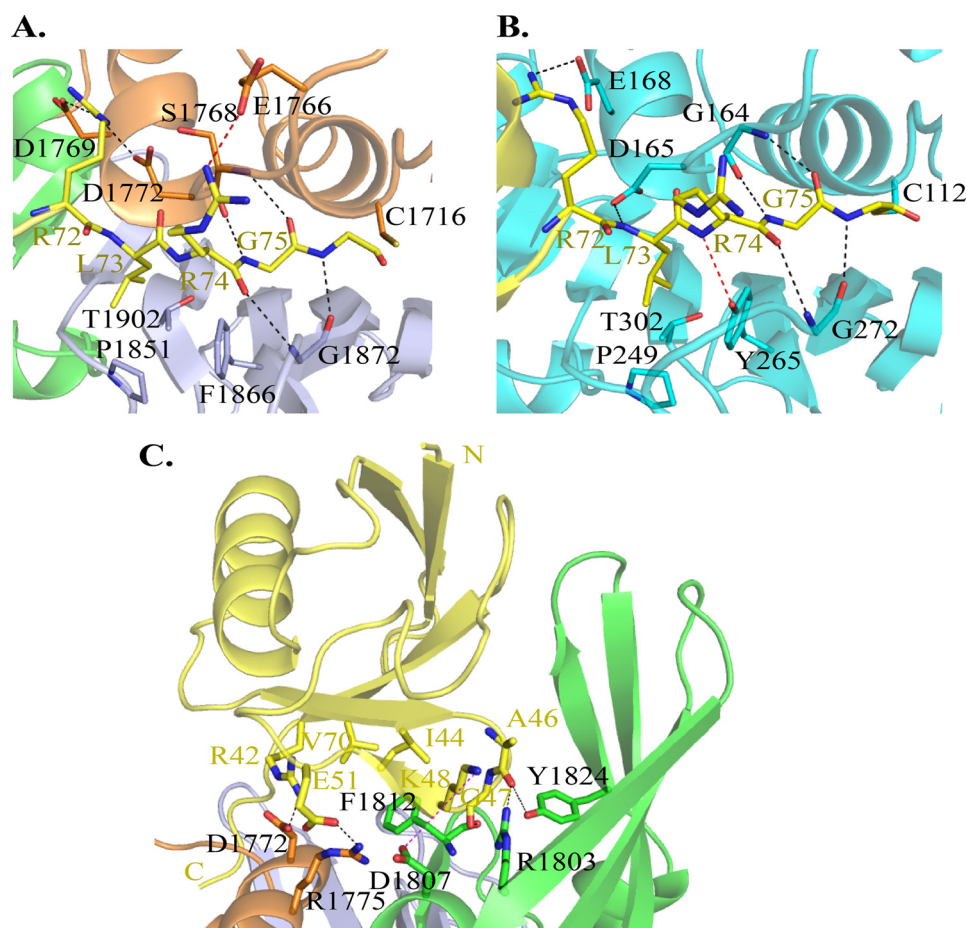


FIGURE 5. **Model of PLP2 in complex with Ub.** A and B, potential interactions between PLP2 and the C-terminal residues of Ub (A) in comparison with the identified interactions between SARS-CoV PLpro and the C-terminal residues of Ub (B) as observed in the structure of SARS-CoV PLpro-Ub complex (PDB code 4MM3). PLP2 is colored as in Fig. 3: thumb (orange), palm (light blue), and fingers (green). Ub is shown in yellow, and SARS-CoV PLpro is shown in cyan. Hydrogen bonding and salt bridge interactions are represented as dashed lines. The red dashed line in A indicates that a similar interaction is not observed in B, and vice versa. C, potential interactions between PLP2 and Ub (yellow). Only the interactions that persist for more than 50% of the simulation time are shown. The magenta dashed line indicates that the interaction persists for more than 50% of the simulation time but is not present in the current analyzed frame.

Ile<sup>44</sup>–Val<sup>70</sup> hydrophobic patch of Ub. Moreover, residues Asp<sup>1772</sup>, Arg<sup>1775</sup>, and Asp<sup>1807</sup> each engage in salt bridge interactions with Arg<sup>42</sup>, Glu<sup>51</sup>, and Lys<sup>48</sup>, respectively. The more complementary charge contacts that exist in the MHV PLP2-Ub complex but not the SARS-CoV PLpro-Ub complex may account for the much lower  $K_m$  of PLP2+ with Ub-AMC than that of SARS-CoV PLpro.

**Mutagenesis Studies of MHV PLP2+ Reveal Important Residues Involved in Ub Binding and Interferon Antagonism**—To probe the importance of identified residues in Ub binding, we performed mutagenesis studies and characterized the activities of the resulting mutants with substrates Z-RLRGG-AMC and Ub-AMC. As summarized in Table 3, the D1772R mutant has only 1% of WT activity with Ub-AMC, whereas 50% of WT activity with Z-RLRGG-AMC is maintained. The same trend is observed with the D1807R mutant. These observations suggest that both Asp<sup>1772</sup> and Asp<sup>1807</sup> of MHV PLP2 play important roles in binding Ub via regions outside of the Ub C terminus. Asp<sup>1807</sup> is poorly conserved among CoVs (Fig. 6), implying that the interaction between Asp<sup>1807</sup> and Ub may be unique to MHV PLP2. On the other hand, residues corresponding to Asp<sup>1772</sup> in MHV PLP2 are either aspartic or glutamic acids in other CoVs (Fig. 6), except MERS-CoV PLpro (arginine) and IBV PLP2

**TABLE 3**  
Activity characterization of PLP2+ mutants

	Relative activity of WT	
	50 $\mu$ M RLRGG-AMC	500 nM Ub-AMC
WT	100 $\pm$ 3	100 $\pm$ 2
D1772R	42.1 $\pm$ 2.4	1.1 $\pm$ 0.1
D1807R	26.2 $\pm$ 2.0	0.5 $\pm$ 0.1
Y1824F	46.2 $\pm$ 0.7	70.3 $\pm$ 4.4
Y1824A	0	3.0 $\pm$ 0.2
F1812A	41.1 $\pm$ 0.9	3.3 $\pm$ 0.9

(tryptophan). In fact, Glu<sup>168</sup>, which corresponds to Asp<sup>1772</sup> in SARS-CoV PLpro has also been shown to be important for interacting with Ub (55). However, the observation that MERS-CoV PLpro also has a comparable level of DUB activity (29) suggests that this enzyme may interact with Ub in a different manner.

Two mutants, Y1824F and Y1824A, were generated to investigate the role of the phenolic side chain in ubiquitin binding. Whereas the Y1824F mutant was found to possess activities comparable with those of WT, the Y1824A mutant is essentially inactive. This indicates that the predicted hydrogen-bonding interaction between Tyr<sup>1824</sup> and Ub is not crucial for the processing of Ub. However, the presence of an aromatic ring at this

## Structure of Three Tandemly Linked Domains of MHV nsp3

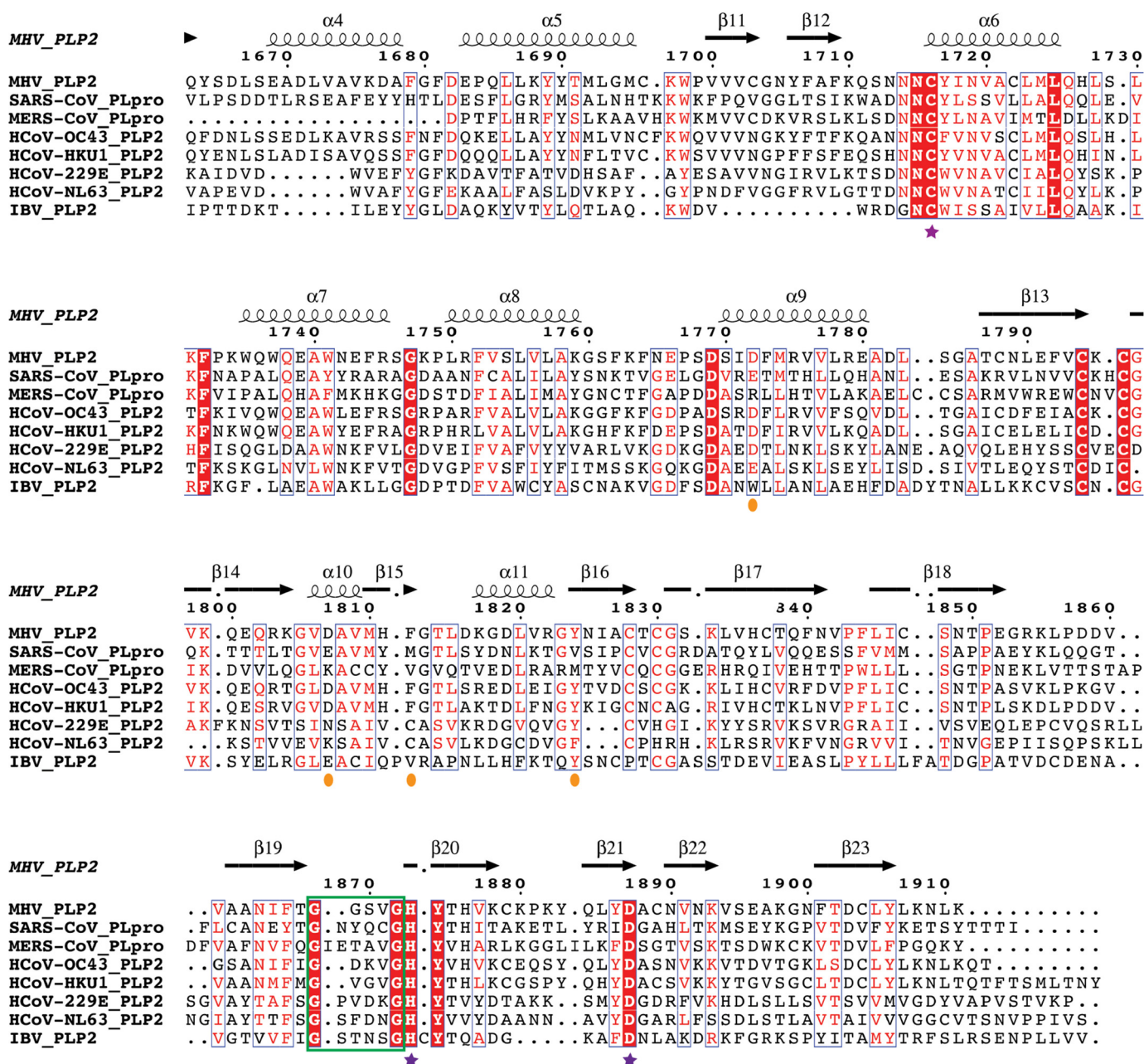


**FIGURE 6. Sequence alignment of various coronavirus PLP2s.** Group 1, HCoV-229E and HCoV-NL63; group 2, MHV, SARS-CoV, MERS-CoV, HCoV-OC43, and HCoV-HKU1; group 3, IBV. The BL2 loop residues are boxed in green. Purple stars, catalytic triad residues; orange ovals, residues of MHV PLP2 that may be involved in important interactions with Ub. Accession numbers are as follows: MHV PLP2, P0C6V0; SARS-CoV PLpro, AEA10816.1; MERS-CoV PLpro, YP\_007188578.1; HCoV-OC43, NP\_937947.21; HCoV-HKU1, YP\_460024.1; HCoV-229E, AGT21365.1; HCoV-NL63, AFD98832.1; IBV, P0C6V5.1. The alignment was performed using Clustal Omega. The figure was generated using ESPript (67). Same residues are shaded in red, and conserved residues are shown in red.

position is important, given the packing around the Tyr<sup>1824</sup> residue (Fig. 7A), and its removal may compromise the protein's stability and thus its enzymatic activity (Table 3). Indeed, temperature inactivation experiments show that Y1824A is much more unstable than Y1824F (Fig. 7C). Interestingly, the multiple sequence alignment of various PLPs reveals that residues at this position are conserved as mainly aromatic or in one case a methionine (Fig. 6).

Importantly, the F1812A mutant leads to a substantial decrease (3% remaining activity) in its DUB activity, whereas 50% of its activity with Z-RLRGG-AMC is maintained. This

indicates that the hydrophobic interaction between Phe<sup>1812</sup> and the Ile<sup>44</sup>-Val<sup>70</sup> patch is important in the recognition of Ub. Given the packing of Phe<sup>1812</sup> against Ile<sup>44</sup>-Val<sup>70</sup> (Fig. 7B), it is not surprising that the replacement of Phe<sup>1812</sup> with alanine has such dire consequences to its DUB activity. Notably, most CoVs have conserved hydrophobic residues at this position (Fig. 6).

Finally, to investigate the correlation between the DUB activity of PLP2 and its ability to antagonize IFN production, we performed IFN antagonism assays in cell culture with several selected mutants. In particular, the Y1824F mutant, which displays WT level DUB activity, preserves the ability to antagonize

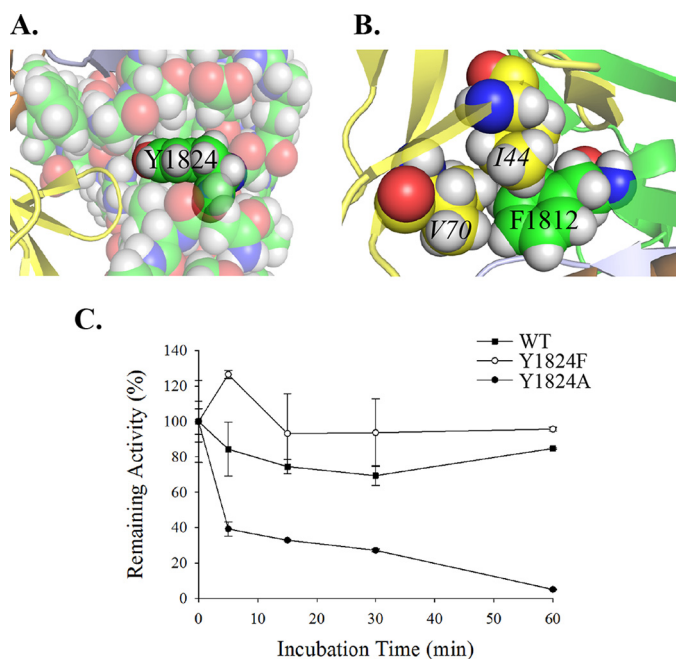


**FIGURE 7. Packing of MHV PLP2 around residues Tyr<sup>1824</sup> and Phe<sup>1812</sup>.** *A*, the packing of the PLP2 fingers domain around Tyr<sup>1824</sup> shown in a space-filling view (green, carbon; red, oxygen; blue, nitrogen; gray, hydrogen). Ub is shown as a cartoon in yellow. *B*, the packing of Phe<sup>1812</sup> from PLP2 against the Ile<sup>44</sup>-Val<sup>70</sup> patch from Ub shown in a space-filling view. The color code is the same as in *A*, except carbon atoms of Ile<sup>44</sup> and Val<sup>70</sup> are shown in yellow. *C*, temperature inactivation of PLP2+ mutant Y1824A. The activity of WT PLP2+ and two PLP2+ mutants (Y1824F and Y1824A) were measured after incubation at 30 °C for different time periods and then normalized to the activity at 0 min. Error bars, S.D.

IFN production, whereas the inactive mutant, Y1824A, loses IFN antagonism ability (Fig. 8). In contrast to Y1824F, the D1772R, D1807R, and F1812A mutants, which have moderate activities against Z-RLRGG-AMC but low DUB activities, are unable to block the activation of IFN (Fig. 8). Thus, the combined computational modeling and enzyme kinetic studies aid in the identification of regions and residues important for ubiquitin binding and IFN antagonism.

## Discussion

In this study, we demonstrate that purified MHV PLP2+ has both deubiquitinating and deISGylating activities, with the former activity being the most dominant. A survey of various ubiquitin linkages shows that PLP2+ processes the isopeptide bonds of di-Ubs of all types, with the exception of linear di-Ub, which contains a peptide bond. We also report the first crystal structure of the PLP2 catalytic core together with two of its N-terminal adjacent domains as part of nsp3. Besides the expected thumb-palm-finger architecture of the PLP2 catalytic core and the Ubl2 domain at its N terminus, the x-ray structure reveals a domain preceding the Ubl2 domain in MHV nsp3 that is so far only similar to the SARS-CoV SUD-C domain. We designate this domain as the DPUP (domain preceding Ubl2 and PLP2) domain. Finally, we generated a computational model of PLP2 in complex with Ubal, and supported by mutagenesis studies, we show that the computational model provides insights into the interactions between PLP2 and Ub.

Kinetic characterization of MHV PLP2+ revealed significant distinctions in the deubiquitination and deISGylation activities

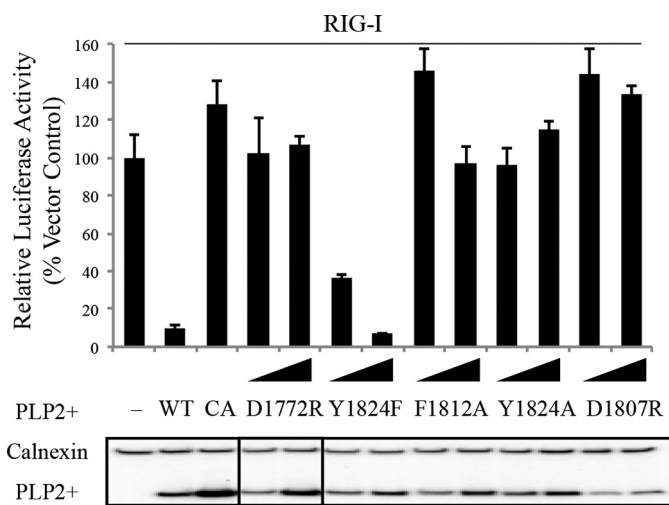


**FIGURE 8. Interferon antagonism activity of MHV PLP2+ wild type and mutants.** HEK293T cells were transfected with plasmids expressing either the WT, the catalytic mutant (CA), or the indicated PLP2+ mutants and plasmids expressing IFN $\beta$ -luc, Renilla-luc, and N-RIG-I. At 16 h post-transfection, cells were lysed, and luciferase activity was measured. Experiments were performed in triplicate. Error bars, S.D.

of MHV PLP2+ and SARS-CoV PLpro. The results suggest that these two viral proteins may target different cellular substrates to facilitate viral evasion of the host innate immune responses. Furthermore, the fact that MHV PLP2+ can process di-Ubs of all linkage types, except the linear one, indicates that this enzyme displays promiscuous recognition surrounding the environment of the lysine residue of the proximal ubiquitin molecule in ubiquitin chains. What is not clear is whether or not there are specific substrate recognition mechanisms associated with MHV PLP2+ that are mediated through the interactions with specific ubiquitinated substrates instead of the attached ubiquitin chains. Alternatively, MHV PLP2+ may require external assistance, such as other domains in nsp3, to achieve substrate discrimination, or MHV PLP2+ may indiscriminately deubiquitinate multiple host cell proteins. Moreover, the observation that MHV PLP2+ can process both Lys<sup>48</sup>- and Lys<sup>63</sup>-linked polyubiquitin chains to monoubiquitin with nearly equal efficiency differs from that of SARS-CoV PLpro. In the case with SARS-CoV PLpro, Lys<sup>48</sup>-linked ubiquitin chains are cleaved much more rapidly than the Lys<sup>63</sup>-linked ones, and Lys<sup>48</sup>-di-Ub is processed much slower than the longer ubiquitin chains (26). This observed difference indicates that, unlike SARS-CoV PLpro, which has two ubiquitin binding sites (40), MHV PLP2+ most likely has only one ubiquitin binding site.

Of significant importance is the discovery of the DPUP domain in MHV nsp3 as revealed by the x-ray structure of PLP2+. The SUD, including SUD-N, SUD-M, and SUD-C, was believed to be unique to SARS-CoV and, perhaps, responsible for its extreme pathogenicity (24). Subsequently, Neuman *et al.* (12) performed a bioinformatics analysis of nsp3s from multiple coronaviruses and proposed that the SUD-C exists only in the  $\beta$ -coronavirus genogroups 2b, 2c, and 2d and not in genogroup 2a, to which MHV belongs. In addition, the SUD-C is predicted to be absent in the  $\alpha$ - and  $\gamma$ -coronaviruses. X-ray and NMR structural studies show that subdomains SUD-N and SUD-M

## Structure of Three Tandemly Linked Domains of MHV nsp3

adopt macrodomain folds, whereas SUD-C adopts a frataxin-like fold (15, 16). Interestingly, SUD-NM and its individual subdomains can bind oligonucleotides that form G-quadruplexes (15, 56). SUD-C has also been shown to have RNA-binding ability, and concerted actions by the subdomains of SUD have been proposed to ensure specific RNA binding (16). We have attempted to investigate the ability of the DPUP domain to bind oligonucleotides; however, the results were inconclusive (data not shown). Nonetheless, the presence of the DPUP domain in MHV nsp3 and the bioinformatics prediction suggest that SUD should no longer be considered “unique” to SARS-CoV. Therefore, it is intriguing to investigate the presence of similar domains in other CoVs and their roles in virus infection, replication, and pathogenesis.

The computational model of PLP2 in complex with Ubal provides insights into the molecular interactions between the enzyme and its ubiquitin substrates and helps in providing a structural rationale for the results of the kinetic characterization. The extensive interactions predicted between PLP2 and the Ub beyond the -RLRGG C-terminal sequence may account for the significantly higher activity of PLP2+ with Ub-AMC than with the Z-RLRGG pentapeptide substrate. A higher extent of charge complementarity between PLP2 and Ub, compared with that displayed by SARS-CoV PLpro, may explain the much lower  $K_m$  of the former with Ub-AMC. Mutagenesis of PLP2+ supports the model and, at the same time, reveals the importance of residues Asp<sup>1772</sup>, Asp<sup>1807</sup>, Tyr<sup>1824</sup>, and Phe<sup>1812</sup> in the recognition of Ub. To evaluate the role of PLP2 DUB activity in immune evasion in the context of virus replication through the approach of protein engineering, it is essential to maintain the proteolytic activity of the mutants. The residues listed above, which are located away from the active site, can serve as candidates for protein engineering of PLP2 in an effort to selectively disrupt its DUB activity and, therefore, its IFN antagonism ability.

Coronaviral nsp3 is a large, membrane-associated, multidomain protein. SARS-CoV nsp3 has been shown to play a crucial role in inducing the formation of double-membrane vehicles (57). Furthermore, a proteomics analysis of SARS-CoV virions has described nsp3 as the “hub of connectivity” because it makes the most interactions with other viral proteins, implying a critical role of nsp3 in virion assembly and virus replication (12, 20). Although several domains of nsp3 have been characterized individually, including the ADRP domain (from SARS-CoV and HCoV-229E), the PLP domain (from SARS-CoV, HCoV-NL63, MERS-CoV, TGEV, and porcine epidemic diarrhea virus), and the SARS-CoV SUD domain (15–17, 26, 56, 58), it remains unclear how nsp3 coordinates the multiple domains with different functions to participate in viral RNA synthesis and whether there are any concerted actions among domains. For example, our recent study revealed the critical role of the Ubl2 domain adjacent to PLP2 in maintaining the stability and activity of the protease (23). We found that mutations in the Ubl2 domain resulted in a temperature-sensitive phenotype and that the virus was highly attenuated in animals. In addition, this Ubl2 mutant induced protective immunity and provided a new approach to vaccine development for coronaviruses. Because of the potential cross-talk between the adja-

cent domains, it would be important to characterize nsp3 kinetically and structurally in its entirety and to evaluate the function of each domain in the context of full nsp3. Toward this goal, we disclose herein the enzymatic and structural characterization of the largest portion of coronaviral nsp3 that has ever been studied *in vitro*, which consists of the DPUP domain, the Ubl domain, and the PLP2 domain.

Although PLP2 has been shown to be capable of deubiquitinating TBK1 in cell-based assays (38), here the DUB activity of PLP2 is explicitly validated through *in vitro* characterization using purified recombinant proteins. Antagonizing the host innate immune responses through viral deubiquitinating/deISGylating enzymes is a common strategy employed by viruses. Besides coronaviruses, other species, such as adenovirus, nairovirus, arterivirus, and herpesvirus, have also been found to encode proteases that have deubiquitinating/deISGylating activities, and these proteases are proposed to assist in evading ubiquitin- or ISG15-dependent host innate immune responses (59–61). Extensive protein overexpression studies performed on cellular levels have to some extent supported this hypothesis (33, 35, 39). Moreover, studies with equine arteritis virus PLP2 have shown that cells infected with DUB activity-deficient equine arteritis virus display significantly enhanced innate immune responses compared with cells infected with WT virus (62). However, a detailed mechanism of how viral DUBs suppress host immune responses is still not fully clear.

The continuous emergence of severe epidemics caused by new CoVs requires better understanding of the infection and pathogenesis mechanisms. MHV is the best-studied coronavirus model, and it has an undeniable advantage of ease in culturing in comparison with HCoVs. The discovery that PLP2 has deubiquitinating/deISGylating activities enables the use of MHV as a model to study the mechanism of coronavirus immune evasion through viral DUBs. More importantly, the structure of PLP2 and the model of PLP2-Ub complex provided by this study bring us closer to this goal.

---

*Author Contributions*—Y. C. and A. D. M. conceived and coordinated the study and wrote the paper. Y. C. purified, characterized, and crystallized PLP2+ and determined its x-ray structure. S. N. S. built the computation model of PLP2-Ub complex. Y. C. and S. N. S. designed the mutants. Y. C. and T. C. purified and characterized the mutants. A. M. M. designed, performed, and analyzed the experiments shown in Fig. 8. S. C. B. provided substantial contributions to analysis and interpretation of data. All authors reviewed the results and approved the final version of the manuscript.

---

*Acknowledgments*—We thank Dr. Lake Paul (Purdue Bindley Bioscience Center) for assistance with size exclusion chromatography/multiangle light scattering data collection and analysis and Paola C. Montenegro for help with the purification of PLP2+ mutants. We also thank the CCP4 workshop 2013, and the personnel of the Advanced Photon Source Life Science-Collaborative Access Team and National Institutes of General Medical Sciences and Cancer for assistance in data collection and processing.

---

## References

1. Graham, R. L., Donaldson, E. F., and Baric, R. S. (2013) A decade after SARS: strategies for controlling emerging coronaviruses. *Nat. Rev. Micro-*

- biol.* **11**, 836–848
- Peiris, J. S., Yuen, K. Y., Osterhaus, A. D., and Stöhr, K. (2003) The severe acute respiratory syndrome. *N. Engl. J. Med.* **349**, 2431–2441
  - World Health Organization (2015) Middle East Respiratory Syndrome coronavirus (MERS-CoV): Saudi Arabia: Disease Outbreak News, World Health Organization, Geneva
  - Li, W., Shi, Z., Yu, M., Ren, W., Smith, C., Epstein, J. H., Wang, H., Cramer, G., Hu, Z., Zhang, H., Zhang, J., McEachern, J., Field, H., Daszak, P., Eaton, B. T., Zhang, S., and Wang, L. F. (2005) Bats are natural reservoirs of SARS-like coronaviruses. *Science* **310**, 676–679
  - Memish, Z. A., Mishra, N., Olival, K. J., Fagbo, S. F., Kapoor, V., Epstein, J. H., Alhakeem, R., Durosinloun, A., Al Asmari, M., Islam, A., Kapoor, A., Briese, T., Daszak, P., Al Rabeeah, A. A., and Lipkin, W. I. (2013) Middle East respiratory syndrome coronavirus in bats, Saudi Arabia. *Emerg. Infect. Dis.* **19**, 1819–1823
  - Haagmans, B. L., Al Dhahiry, S. H., Reusken, C. B., Raj, V. S., Galiano, M., Myers, R., Godeke, G. J., Jonges, M., Farag, E., Diab, A., Ghobashy, H., Alhajri, F., Al-Thani, M., Al-Marri, S. A., Al Romaihi, H. E., Al Khal, A., Bermingham, A., Osterhaus, A. D., AlHajri, M. M., and Koopmans, M. P. (2014) Middle East respiratory syndrome coronavirus in dromedary camels: an outbreak investigation. *Lancet Infect. Dis.* **14**, 140–145
  - Cima, G. (2014) PED virus reinfected U.S. herds. Virus estimated to have killed 7 million-plus pigs. *J. Am. Vet. Med. Assoc.* **245**, 166–167
  - Gosert, R., Kanjanahaluthai, A., Egger, D., Bienz, K., and Baker, S. C. (2002) RNA replication of mouse hepatitis virus takes place at double-membrane vesicles. *J. Virol.* **76**, 3697–3708
  - Ziebuhr, J., Snijder, E. J., and Gorbalenya, A. E. (2000) Virus-encoded proteinases and proteolytic processing in the Nidovirales. *J. Gen. Virol.* **81**, 853–879
  - Ziebuhr, J. (2006) The coronavirus replicase: insights into a sophisticated enzyme machinery. *Adv. Exp. Med. Biol.* **581**, 3–11
  - Knoops, K., Kikkert, M., Worm, S. H., Zevenhoven-Dobbe, J. C., van der Meer, Y., Koster, A. J., Mommaas, A. M., and Snijder, E. J. (2008) SARS-coronavirus replication is supported by a reticulovesicular network of modified endoplasmic reticulum. *PLoS Biol.* **6**, e226
  - Neuman, B. W., Joseph, J. S., Saikatendu, K. S., Serrano, P., Chatterjee, A., Johnson, M. A., Liao, L., Klaus, J. P., Yates, J. R., 3rd, Wüthrich, K., Stevens, R. C., Buchmeier, M. J., and Kuhn, P. (2008) Proteomics analysis unravels the functional repertoire of coronavirus nonstructural protein 3. *J. Virol.* **82**, 5279–5294
  - Serrano, P., Johnson, M. A., Almeida, M. S., Horst, R., Herrmann, T., Joseph, J. S., Neuman, B. W., Subramanian, V., Saikatendu, K. S., Buchmeier, M. J., Stevens, R. C., Kuhn, P., and Wüthrich, K. (2007) Nuclear magnetic resonance structure of the N-terminal domain of nonstructural protein 3 from the severe acute respiratory syndrome coronavirus. *J. Virol.* **81**, 12049–12060
  - Saikatendu, K. S., Joseph, J. S., Subramanian, V., Clayton, T., Griffith, M., Moy, K., Velasquez, J., Neuman, B. W., Buchmeier, M. J., Stevens, R. C., and Kuhn, P. (2005) Structural basis of severe acute respiratory syndrome coronavirus ADP-ribose-1<sup>st</sup>-phosphate dephosphorylation by a conserved domain of nsP3. *Structure* **13**, 1665–1675
  - Tan, J., Vonrhein, C., Smart, O. S., Bricogne, G., Bollati, M., Kusov, Y., Hansen, G., Mesters, J. R., Schmidt, C. L., and Hilgenfeld, R. (2009) The SARS-unique domain (SUD) of SARS coronavirus contains two macrodomains that bind G-quadruplexes. *PLoS Pathog.* **5**, e1000428
  - Johnson, M. A., Chatterjee, A., Neuman, B. W., and Wüthrich, K. (2010) SARS coronavirus unique domain: three-domain molecular architecture in solution and RNA binding. *J. Mol. Biol.* **400**, 724–742
  - Ratia, K., Saikatendu, K. S., Santarsiero, B. D., Barretto, N., Baker, S. C., Stevens, R. C., and Mesecar, A. D. (2006) Severe acute respiratory syndrome coronavirus papain-like protease: structure of a viral deubiquitinating enzyme. *Proc. Natl. Acad. Sci. U.S.A.* **103**, 5717–5722
  - Serrano, P., Johnson, M. A., Chatterjee, A., Neuman, B. W., Joseph, J. S., Buchmeier, M. J., Kuhn, P., and Wüthrich, K. (2009) Nuclear magnetic resonance structure of the nucleic acid-binding domain of severe acute respiratory syndrome coronavirus nonstructural protein 3. *J. Virol.* **83**, 12998–13008
  - Fehr, A. R., Athmer, J., Channappanavar, R., Phillips, J. M., Meyerholz, D. K., and Perlman, S. (2015) The nsp3 macrodomain promotes virulence in mice with coronavirus-induced encephalitis. *J. Virol.* **89**, 1523–1536
  - Hurst, K. R., Koetzner, C. A., and Masters, P. S. (2013) Characterization of a critical interaction between the coronavirus nucleocapsid protein and nonstructural protein 3 of the viral replicase-transcriptase complex. *J. Virol.* **87**, 9159–9172
  - Hurst-Hess, K. R., Kuo, L., and Masters, P. S. (2015) Dissection of amino-terminal functional domains of murine coronavirus nonstructural protein 3. *J. Virol.* **89**, 6033–6047
  - Keane, S. C., and Giedroc, D. P. (2013) Solution structure of mouse hepatitis virus (MHV) nsp3a and determinants of the interaction with MHV nucleocapsid (N) protein. *J. Virol.* **87**, 3502–3515
  - Mielech, A. M., Deng, X., Chen, Y., Kindler, E., Wheeler, D. L., Mesecar, A. D., Thiel, V., Perlman, S., and Baker, S. C. (2015) Murine coronavirus ubiquitin-like domain is important for papain-like protease stability and viral pathogenesis. *J. Virol.* **89**, 4907–4917
  - Snijder, E. J., Bredenbeek, P. J., Dobbe, J. C., Thiel, V., Ziebuhr, J., Poon, L. L., Guan, Y., Rozanov, M., Spaan, W. J., and Gorbalenya, A. E. (2003) Unique and conserved features of genome and proteome of SARS-coronavirus, an early split-off from the coronavirus group 2 lineage. *J. Mol. Biol.* **331**, 991–1004
  - Báez-Santos, Y. M., Mielech, A. M., Deng, X., Baker, S., and Mesecar, A. D. (2014) Catalytic function and substrate specificity of the papain-like protease domain of nsp3 from the Middle East respiratory syndrome coronavirus. *J. Virol.* **88**, 12511–12527
  - Barretto, N., Jukneliene, D., Ratia, K., Chen, Z., Mesecar, A. D., and Baker, S. C. (2005) The papain-like protease of severe acute respiratory syndrome coronavirus has deubiquitinating activity. *J. Virol.* **79**, 15189–15198
  - Chen, Z., Wang, Y., Ratia, K., Mesecar, A. D., Wilkinson, K. D., and Baker, S. C. (2007) Proteolytic processing and deubiquitinating activity of papain-like proteases of human coronavirus NL63. *J. Virol.* **81**, 6007–6018
  - Mielech, A. M., Chen, Y., Mesecar, A. D., and Baker, S. C. (2014) Nidovirus papain-like proteases: multifunctional enzymes with protease, deubiquitinating and deISGylating activities. *Virus Res.* **194**, 184–190
  - Mielech, A. M., Kilianski, A., Baez-Santos, Y. M., Mesecar, A. D., and Baker, S. C. (2014) MERS-CoV papain-like protease has deISGylating and deubiquitinating activities. *Virology* **450**, 64–70
  - Wojdyla, J. A., Manolaridis, I., van Kasteren, P. B., Kikkert, M., Snijder, E. J., Gorbalenya, A. E., and Tucker, P. A. (2010) Papain-like protease 1 from transmissible gastroenteritis virus: crystal structure and enzymatic activity toward viral and cellular substrates. *J. Virol.* **84**, 10063–10073
  - Xing, Y., Chen, J., Tu, J., Zhang, B., Chen, X., Shi, H., Baker, S. C., Feng, L., and Chen, Z. (2013) The papain-like protease of porcine epidemic diarrhea virus negatively regulates type I interferon pathway by acting as a viral deubiquitinase. *J. Gen. Virol.* **94**, 1554–1567
  - Lindner, H. A., Lytvyn, V., Qi, H., Lachance, P., Ziomek, E., and Ménard, R. (2007) Selectivity in ISG15 and ubiquitin recognition by the SARS coronavirus papain-like protease. *Arch. Biochem. Biophys.* **466**, 8–14
  - Clementz, M. A., Chen, Z., Banach, B. S., Wang, Y., Sun, L., Ratia, K., Baez-Santos, Y. M., Wang, J., Takayama, J., Ghosh, A. K., Li, K., Mesecar, A. D., and Baker, S. C. (2010) Deubiquitinating and interferon antagonism activities of coronavirus papain-like proteases. *J. Virol.* **84**, 4619–4629
  - Morales, D. J., and Lenschow, D. J. (2013) The antiviral activities of ISG15. *J. Mol. Biol.* **425**, 4995–5008
  - Frieman, M., Ratia, K., Johnston, R. E., Mesecar, A. D., and Baric, R. S. (2009) Severe acute respiratory syndrome coronavirus papain-like protease ubiquitin-like domain and catalytic domain regulate antagonism of IRF3 and NF- $\kappa$ B signaling. *J. Virol.* **83**, 6689–6705
  - Deng, X., Agnihothram, S., Mielech, A. M., Nichols, D. B., Wilson, M. W., StJohn, S. E., Larsen, S. D., Mesecar, A. D., Lenschow, D. J., Baric, R. S., and Baker, S. C. (2014) A chimeric virus-mouse model system for evaluating the function and inhibition of papain-like proteases of emerging coronaviruses. *J. Virol.* **88**, 11825–11833
  - Yang, X., Chen, X., Bian, G., Tu, J., Xing, Y., Wang, Y., and Chen, Z. (2014) Proteolytic processing, deubiquitinase and interferon antagonist activities of Middle East respiratory syndrome coronavirus papain-like protease. *J. Gen. Virol.* **95**, 614–626

## Structure of Three Tandemly Linked Domains of MHV nsp3

38. Wang, G., Chen, G., Zheng, D., Cheng, G., and Tang, H. (2011) PLP2 of mouse hepatitis virus A59 (MHV-A59) targets TBK1 to negatively regulate cellular type I interferon signaling pathway. *PLoS One* **6**, e17192
39. Zheng, D., Chen, G., Guo, B., Cheng, G., and Tang, H. (2008) PLP2, a potent deubiquitinase from murine hepatitis virus, strongly inhibits cellular type I interferon production. *Cell Res.* **18**, 1105–1113
40. Ratia, K., Kilianski, A., Baez-Santos, Y. M., Baker, S. C., and Mesecar, A. (2014) Structural basis for the ubiquitin-linkage specificity and deISGylating activity of SARS-CoV papain-like protease. *PLoS Pathog.* **10**, e1004113
41. Otwinowski, Z., and Minor, W. (1997) Processing of x-ray diffraction data collected in oscillation mode. *Methods Enzymol.* **276**, 307–326
42. Terwilliger, T. C., Adams, P. D., Read, R. J., McCoy, A. J., Moriarty, N. W., Grosse-Kunstleve, R. W., Afonine, P. V., Zwart, P. H., and Hung, L. W. (2009) Decision-making in structure solution using Bayesian estimates of map quality: the PHENIX AutoSol wizard. *Acta Crystallogr. D* **65**, 582–601
43. Emsley, P., and Cowtan, K. (2004) Coot: model-building tools for molecular graphics. *Acta Crystallogr. D Biol. Crystallogr.* **60**, 2126–2132
44. Afonine, P. V., Grosse-Kunstleve, R. W., Echols, N., Headd, J. J., Moriarty, N. W., Mustyakimov, M., Terwilliger, T. C., Urzhumtsev, A., Zwart, P. H., and Adams, P. D. (2012) Towards automated crystallographic structure refinement with phenix.refine. *Acta Crystallogr. D Biol. Crystallogr.* **68**, 352–367
45. Langer, G., Cohen, S. X., Lamzin, V. S., and Perrakis, A. (2008) Automated macromolecular model building for x-ray crystallography using ARP/wARP version 7. *Nat. Protoc.* **3**, 1171–1179
46. Andreeva, A., Howorth, D., Brenner, S. E., Hubbard, T. J., Chothia, C., and Murzin, A. G. (2004) SCOP database in 2004: refinements integrate structure and sequence family data. *Nucleic Acids Res.* **32**, D226–D229
47. Holm, L., and Rosenström, P. (2010) Dali server: conservation mapping in 3D. *Nucleic Acids Res.* **38**, W545–W549
48. Holm, L., and Park, J. (2000) DaliLite workbench for protein structure comparison. *Bioinformatics* **16**, 566–567
49. Giles, N. M., Watts, A. B., Giles, G. I., Fry, F. H., Littlechild, J. A., and Jacob, C. (2003) Metal and redox modulation of cysteine protein function. *Chem. Biol.* **10**, 677–693
50. Ratia, K., Pegan, S., Takayama, J., Sleeman, K., Coughlin, M., Baliji, S., Chaudhuri, R., Fu, W., Prabhakar, B. S., Johnson, M. E., Baker, S. C., Ghosh, A. K., and Mesecar, A. D. (2008) A noncovalent class of papain-like protease/deubiquitinase inhibitors blocks SARS virus replication. *Proc. Natl. Acad. Sci. U.S.A.* **105**, 16119–16124
51. Ghosh, A. K., Takayama, J., Rao, K. V., Ratia, K., Chaudhuri, R., Mulhearn, D. C., Lee, H., Nichols, D. B., Baliji, S., Baker, S. C., Johnson, M. E., and Mesecar, A. D. (2010) Severe acute respiratory syndrome coronavirus papain-like novel protease inhibitors: design, synthesis, protein-ligand x-ray structure and biological evaluation. *J. Med. Chem.* **53**, 4968–4979
52. Báez-Santos, Y. M., Barraza, S. J., Wilson, M. W., Agius, M. P., Mielech, A. M., Davis, N. M., Baker, S. C., Larsen, S. D., and Mesecar, A. D. (2014) X-ray structural and biological evaluation of a series of potent and highly selective inhibitors of human coronavirus papain-like proteases. *J. Med. Chem.* **57**, 2393–2412
53. Lei, J., Mesters, J. R., Drosten, C., Anemüller, S., Ma, Q., and Hilgenfeld, R. (2014) Crystal structure of the papain-like protease of MERS coronavirus reveals unusual, potentially druggable active-site features. *Antiviral Res.* **109**, 72–82
54. Kong, L., Shaw, N., Yan, L., Lou, Z., and Rao, Z. (2015) Structural view and substrate specificity of papain-like protease from avian infectious bronchitis virus. *J. Biol. Chem.* **290**, 7160–7168
55. Chou, C. Y., Lai, H. Y., Chen, H. Y., Cheng, S. C., Cheng, K. W., and Chou, Y. W. (2014) Structural basis for catalysis and ubiquitin recognition by the severe acute respiratory syndrome coronavirus papain-like protease. *Acta Crystallogr. D Biol. Crystallogr.* **70**, 572–581
56. Tan, J., Kusov, Y., Mutschall, D., Tech, S., Nagarajan, K., Hilgenfeld, R., and Schmidt, C. L. (2007) The “SARS-unique domain” (SUD) of SARS coronavirus is an oligo(G)-binding protein. *Biochem. Biophys. Res. Commun.* **364**, 877–882
57. Angelini, M. M., Akhlaghpour, M., Neuman, B. W., and Buchmeier, M. J. (2013) Severe acute respiratory syndrome coronavirus nonstructural proteins 3, 4, and 6 induce double-membrane vesicles. *MBio* **10**.1128/mBio.00524-13
58. Eglhoff, M. P., Malet, H., Putics, A., Heinonen, M., Dutartre, H., Frangetul, A., Gruez, A., Campanacci, V., Cambillau, C., Ziebuhr, J., Ahola, T., and Canard, B. (2006) Structural and functional basis for ADP-ribose and poly(ADP-ribose) binding by viral macro domains. *J. Virol.* **80**, 8493–8502
59. Frias-Staheli, N., Giannakopoulos, N. V., Kikkert, M., Taylor, S. L., Bridgen, A., Paragas, J., Richt, J. A., Rowland, R. R., Schmaljohn, C. S., Lenschow, D. J., Snijder, E. J., Garcia-Sastre, A., and Virgin, H. W., 4th (2007) Ovarian tumor domain-containing viral proteases evade ubiquitin- and ISG15-dependent innate immune responses. *Cell Host Microbe* **2**, 404–416
60. Isaacson, M. K., and Ploegh, H. L. (2009) Ubiquitination, ubiquitin-like modifiers, and deubiquitination in viral infection. *Cell Host Microbe* **5**, 559–570
61. Lindner, H. A. (2007) Deubiquitination in virus infection. *Virology* **362**, 245–256
62. van Kasteren, P. B., Bailey-Elkin, B. A., James, T. W., Ninaber, D. K., Beugeling, C., Khajehpour, M., Snijder, E. J., Mark, B. L., and Kikkert, M. (2013) Deubiquitinase function of arterivirus papain-like protease 2 suppresses the innate immune response in infected host cells. *Proc. Natl. Acad. Sci. U.S.A.* **110**, E838–E847
63. Piotrowski, Y., Hansen, G., Boomaars-van der Zanden, A. L., Snijder, E. J., Gorbalenya, A. E., and Hilgenfeld, R. (2009) Crystal structures of the X-domains of a Group-1 and a Group-3 coronavirus reveal that ADP-ribose-binding may not be a conserved property. *Protein Sci.* **18**, 6–16
64. Wojdyla, J. A., Manolaridis, I., Snijder, E. J., Gorbalenya, A. E., Coutard, B., Piotrowski, Y., Hilgenfeld, R., and Tucker, P. A. (2009) Structure of the X (ADRP) domain of nsp3 from feline coronavirus. *Acta Crystallogr. D Biol. Crystallogr.* **65**, 1292–1300
65. Bailey-Elkin, B. A., Knaap, R. C., Johnson, G. G., Dalebout, T. J., Ninaber, D. K., van Kasteren, P. B., Bredendiek, P. J., Snijder, E. J., Kikkert, M., and Mark, B. L. (2014) Crystal structure of the Middle East respiratory syndrome coronavirus (MERS-CoV) papain-like protease bound to ubiquitin facilitates targeted disruption of deubiquitinating activity to demonstrate its role in innate immune suppression. *J. Biol. Chem.* **289**, 34667–34682
66. DeLano, W. L. (2014) *The PyMOL Molecular Graphics System*, Version 1.7.2.1, Schrödinger, LLC, New York
67. Robert, X., and Guet, P. (2014) Deciphering key features in protein structures with the new ENDscript server. *Nucleic Acids Res.* **42**, W320–W324